EFFECT OF CRYSTAL MORPHOLOGY ON ELECTRICAL PROPERTIES OF THERMOPLASTIC POLYURETHANE CARBON NANOFIBER COMPOSITE FOR USE IN RAIL FREIGHT SERVICE

A Thesis

by

ANTHONY VILLARREAL

Submitted to the Graduate College of
The University of Texas Rio Grande Valley
In partial fulfillment of the requirements for the degree of

MASTER OF SCIENCE IN ENGINEERING

August 2019

Major Subject: Mechanical Engineering

EFFECT OF CRYSTAL MORPHOLOGY ON ELECTRICAL PROPERTIES OF THERMOPLASTIC POLYURETHANE CARBON NANOFIBER COMPOSITE FOR USE IN RAIL FREIGHT SERVICE

A Thesis
by
ANTHONY VILLARREAL

COMMITTEE MEMBERS

Dr. Constantine Tarawneh
Chair of Committee

Dr. Robert Jones
Co-Chair of Committee

Dr. Arturo Fuentes
Committee Member

August 2019

ABSTRACT

Villarreal, Anthony Alex, Prototyping a Conductive Polymer Steering Pad for Rail Freight Service: Effect Of Crystal Morphology On Electrical, Thermal, And Mechanical Properties Of Thermoplastic Polyurethane Carbon Nanofiber Composite. Master of Science in Engineering (MSE), August, 2019, 64 pp., 10 tables, 40 figures, 22 references

The AdapterPlus™ steering pad is a polymer component on a railcar that helps to reduce stresses on the axle as a railcar rounds a curve. Currently, two copper studs are inserted into the pad to provide a conductive path for the transfer of electronic signals between the railcar and track. However, after continuous cyclic loading caused by normal service operation, the copper studs deform, wear, and eventually lose contact between the two surfaces rendering the pad nonconductive. One proposed solution to this problem is to create a steering pad made entirely from an electrically conductive material. The University Transportation Center for Railway Safety (UTCRS) research team has successfully injection-molded a conductive nanocomposite insert made from vapor grown carbon nanofibers and a modified form of Elastollan 1195A thermoplastic polyurethane (TPU). The injection-molded insert was designed, manufactured, and incorporated into the existing steering pad for further testing. The electrical transport properties of the material were examined using an NI DAQ and servo hydraulic MTS. The morphology of the composite was examined via XRD, SEM, and DSC. It was determined that a conductive composite could be injection-injection molded with a resistivity of around 390 Ω cm depending on the loading and voltage conditions.

DEDICATION

This work is dedicated to my loving family and to all the friends I have had the honor of meeting throughout the years. My father, Oscar, for teaching me to work hard and persevere. My mother, Hilda, for her unwavering support. And my grandmother and aunt, Maria and Geno, who loved and raised me. I would not be who I am, without any of you.

To my friends, for always offering encouragement, laughs, and adventures, I cannot thank you enough.

ACKNOWLEDGEMENTS

I would like to thank my research advisor, Dr. Constantine Tarawneh, for the hard work and long hours that he has invested into this research team. You unselfishly take pride in the success of each student, and foster an environment for growth.

I would also like to thank Dr. Robert Jones for seeing something special in the kid from Radio Shack. Without you, my path would be quite different.

Finally, this study was made possible by funding provided by The University Transportation Center for Railway Safety (UTCRS), through a USDOT Grant No. #DTRT 13-G-UTC59

DISCLAIMER

The contents of this thesis reflect the views of the authors, who are responsible for the facts and the accuracy of the information presented herein. This document is disseminated under the sponsorship of the U.S. Department of Transportation's University Transportation Centers Program, in the interest of information exchange. The U.S. Government assumes no liability for the contents or use thereof.

TABLE OF CONTENTS

Page

LIST OF TABLES

Page

LIST OF FIGURES

Page

CHAPTER I

BACKGROUND & INTRODUCTION

1.1 Introduction

The AdapterPlus™ steering pad, shown in Figure 1, is a polymer component of a rail car that "improves axle to rail wheelset alignment" [1], and in doing so, reduces stress on the axle, and wear of the side frame pedestal. It does this by allowing each side of the wheelset to independently shift and adjust to the track as the railcar rounds a curve. The translation of the wheelset is transformed into deformation of the polymer pad, rather than a buildup of stress within the axle, and wear on mating surfaces when compared to standard metal bearing adapters. The pad is injection-molded using a Thermoplastic Polyurethane (TPU) due to the polymer's elasticity and durability. Two copper studs are molded into the pad to provide a conductive path for electrical signals to be passed via the rail in order to actuate loading devices on the car.

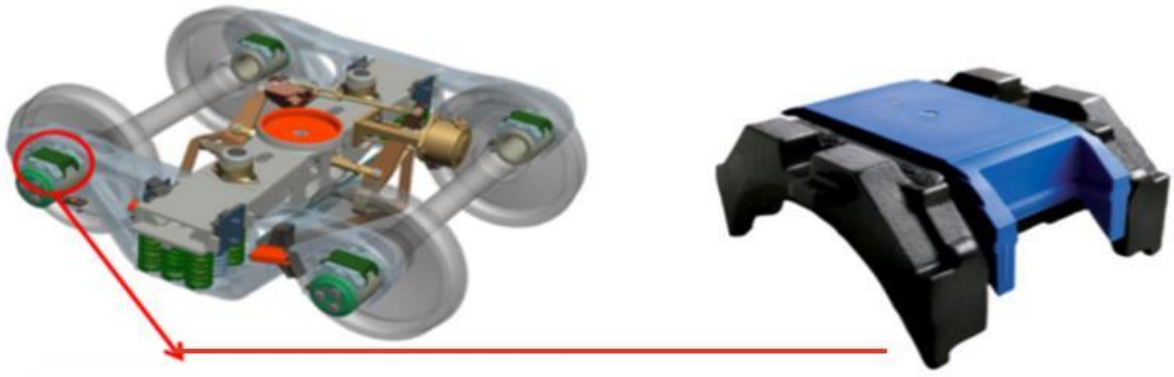

Figure 1. AdapterPlus™ Steering Pad

However, because copper is a soft metal, the studs are easily deformed by cyclic loading and unloading of the car and abrasion from the shifting loads. If the copper studs experience excessive deformation or wear (Figure 2), they lose continuity between the rail and the car, halting communications. A potential solution is to create a homogenous conductive material by blending carbon nanofibers (CNFs) and TPU and using the new composite material as a replacement for the current TPU. This solution would allow electrical signals to travel through the entirety of the pad, instead of being limited to the small area previously occupied by the copper studs.

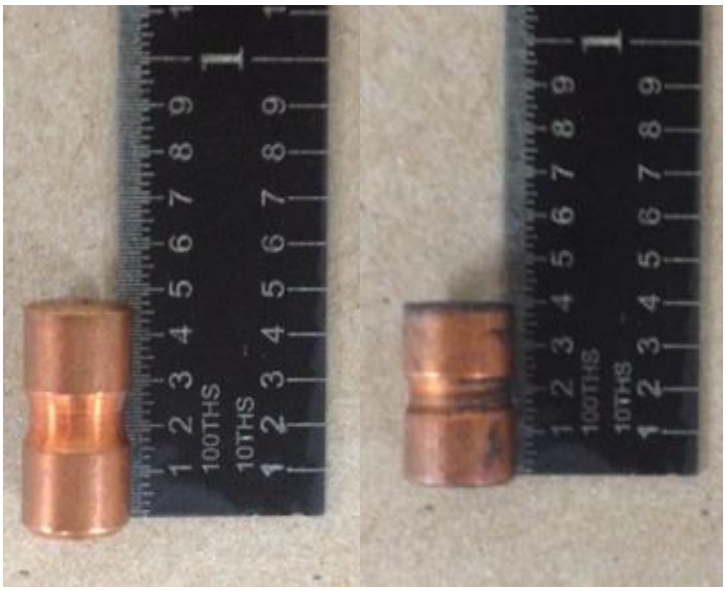

Figure 2. From left to right new copper stud (left) compared to deformed stud (right) [2]

1.2 Previous Work

Two previous researchers have worked at creating a suitable conductive composite for the AdapterPlus™ steering pad. The first was by Ruben Suarez [2], and the second by Daniel Basaldua [3]. In his thesis titled “Design and Optimization of a Railroad Conductive Suspension Element Pad Composed of Thermoplastic Polyurethane and Carbon Black”, Suarez used a blend of carbon black and TPU to create a conductive composite material that was to replace the

standard TPU used in the pad. This material had exceptional electrical conductivity; however, it had poor mechanical properties. In one of his tests, a pad made of the CB/TPU material was placed in a freezer for eight hours then struck with a hammer. After three hits, one leg of the pad completely fractured off. He explains that the carbon black tends to form agglomerates which act as stress risers in the material. The results of the test are shown in Figure 3.

Figure 3. Fractured carbon black/TPU adapter steering pad [2]

In “Effects of Vapor Grown Carbon Nanofibers on Electrical and Mechanical Properties of a Thermoplastic Elastomer”, Basaldua uses carbon nanofibers as the conductive filler in a TPU matrix to create his conductive polymer composite [3]. This material had adequate conductivity for the desired application of actuating a pneumatic valve, and improved mechanical stability when compared to the carbon black counterpart. However, this material failed to remain conductive when it was injection-molded. Based on the appearance of the neat TPU when injection-molded compared to the transfer-molded sample, it was hypothesized that the material did not maintain the same microstructure and therefore did not have the same electrical properties. The work presented in this thesis is an attempt to adjust the composite material developed by Basaldua as well as the injection-molding parameters to obtain an

injection-molded sample that has similar morphology and, therefore, comparable transport properties to the transfer-molded samples.

1.3 Thermoplastic Polyurethane (TPU)

As previously mentioned, the AdapterPlus™ Steering pad is made of a thermoplastic polyurethane (TPU). In order to minimize the changes necessary in the molding process and equipment, TPU was chosen as the matrix for the conductive composite developed in this study. An in-depth review of TPU was made to better understand the behavior of the material and optimize the molding parameters.

Thermoplastic Polyurethane is a subgroup of a wider class of polymers called thermoplastic elastomers (TPEs). In general, TPEs are rubber like materials that can be processed via standard thermoplastic manufacturing techniques such as injection-molding and extrusion. TPEs are composed of both soft and hard segments. The soft segments are often compared to the matrix of a standard polymer composite, whereas the hard segments are compared to the filler or to the crosslinks seen in rubber materials. The two domains are incompatible at room temperature, however, upon melting, the soft and hard segments become homogenous. This leads to the material's favorable processability.

Specifically, TPU is a block copolymer with alternating portions of soft segments, and hard segments [4],[5]. The viscoelastic and damping properties of TPU come from the long, flexible soft segments whereas the strength of the material comes from pinning and crosslinking effects of the hard segments that associate together and form pseudo-crystals to varying degrees, depending on the processing conditions. As previously mentioned, this creates two distinct phases, both a soft and hard phase, within the polymer. The separation of phases is what gives

TPU its good wear performance and toughness, while maintaining a respectably high tensile strength [6]. A schematic of TPU is given in Figure 4.

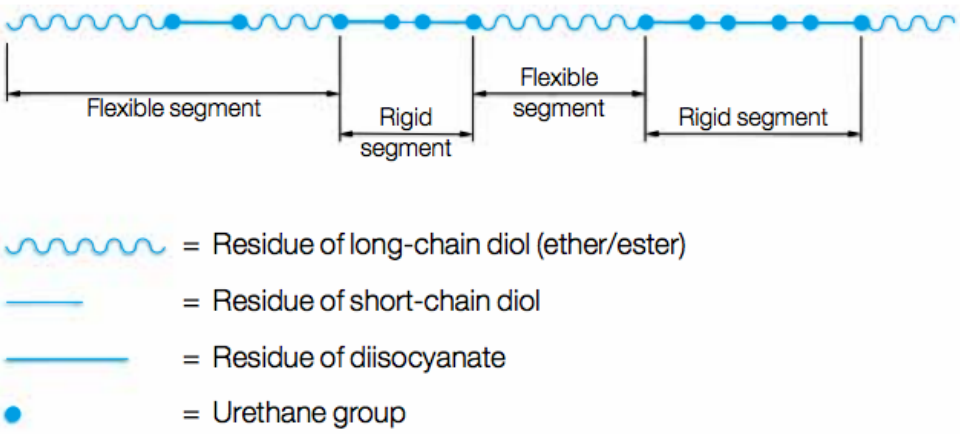

Figure 4. Schematic representation of TPU [6]

TPUs are used in everything from shoe soles to protective cases, and in some instances can even be used as adhesives depending on the chemical makeup. For this project, the composite matrix is a modified version of Ellastollan 1195a provided by BASF that has hard segments that tend to interact with each other faster than the standard version.

1.4 Carbon Nanofibers (CNFs) and Conductive Polymer Fillers

Carbon nanofibers (CNFs) are one-dimensional, cylindrical shaped structures created by arranging layers of graphene, canted at a small angle, one on top of the other as stacked cups. This shape leads to extremely high length-to-diameter ratios, as well as surface area-to-volume ratio [7]. Because the CNFs have such small volumes, they can be compounded into a polymer matrix without adding additional stress to the polymer backbone, which helps to maintain the mechanical properties of the matrix and therefore allow for efficient load transfer between matrix and fibers [8]. Not only that, but the exposed edges of the CNFs can very easily be chemically,

or thermally functionalized to improve chemical bonding between the CNFs and various matrices. Because of graphene's highly ordered structure, the CNFs made from them exhibit excellent mechanical properties, high electrical conductivity, and high thermal conductivity. The mechanical, electrical, and thermal properties of CNFs can be customized through various post production techniques. The CNFs used in this research were Pyrograf® -III PR-19 XT-HHT carbon nanofibers that have been heat treated and functionalized with short range ordered structures to increase the fiber's electrical conductivity [7].

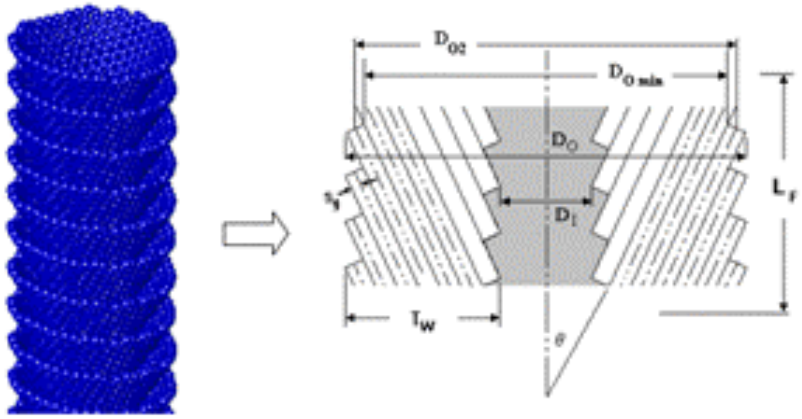

Figure 5. Stacked cup carbon nanofiber [5]

The two mechanisms of electrical conductivity within nanofiber networks are direct contact and tunneling, visually represented in Figure 6. As the name suggests, in direct contact, the fibers in the matrix are physically touching end to end, forming conductive fiber chains throughout the matrix. The electrons are then able to travel down each active fiber chain, and out to the lower-potential side. High electrical conductivity composites can be created through direct contact conductive networks using relatively low fiber percentages, as well as minimal mixing, and therefore lead to a lower cost composite. However, conductive fiber networks formed via direct contact are susceptible to the formation of agglomerates within the polymer due to the need for physical contact of the fibers. The agglomerates act as cracks within the material and

degrade mechanical properties. On the other hand, conductivity via tunneling occurs when fibers are within 10 nano meters of each other. At this distance, the material's potential well, the necessary energy an electron needs to tunnel, is small enough that an energized electron traveling along a fiber can tunnel or, in laymen's terms, "jump" to a neighboring fiber and continue to the zero-potential side. Conductivity via tunneling requires a relatively high percentage of fibers and a well-mixed composite blend, that leads to higher overall manufacturing costs. However, the improved mechanical properties of composites made in this fashion often make conductivity via tunneling the desired method of conductive network formation [8].

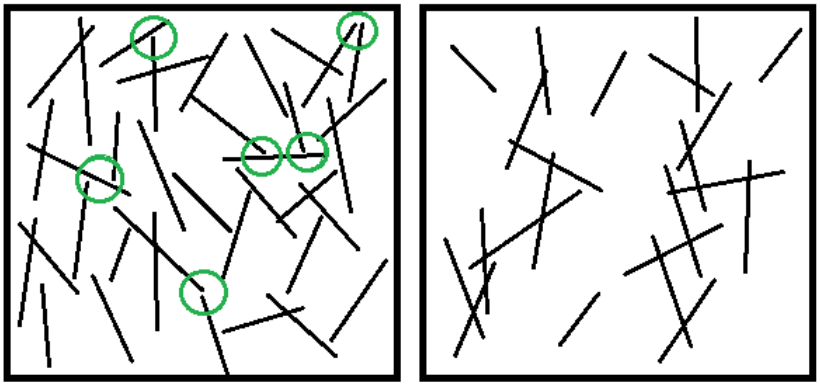

Figure 6.Conductivity via tunneling (left) conductivity via direct contact (right)

Potential alternatives to carbon fiber fillers are carbon black and metal fibers. Compared to carbon nanofiber composites, carbon black composites require a significantly higher concentration of filler to create a conductive material. This high concentration of carbon black often results in a material with low toughness and low wear resistance [2]. Metal fibers are more often seen as a conductive filler in epoxy matrix composites, but are gaining use in standard thermoplastic materials. The challenges with metal fiber composites are that they are much heavier, more difficult to recycle, and can wear manufacturing equipment faster than the other fillers. To counteract the weight and wear issues, softer metals, such as silver, have been used to

coat both glass and CNFs to improve the conductivity of the composite, without drastically increasing the weight, while being less abrasive on manufacturing equipment. A brief summary of the effect of the fiber filler on the thermoplastic composite is provided in Table 1.

Table 1. Comparison of fiber filler and general corresponding composite properties

	Carbon Black	**Carbon Nanofibers**	**Carbon Fiber**	**Metal Fiber**
Composite Stiffness	+	+	+	+
Composite Durability	–	+	+	
Composite Processability	+	+		–
Filler/Fiber Cost	+	–		–

1.5 Applications and Manufacturing of Conductive Polymer Composites (CPCs)

A literature review on the application and manufacturing methods of Conductive Polymer Composites (CPCs) was conducted to become up to date with the latest research, technology, and ideas in the field. The three main papers referenced by this work were “Progress on the morphological control of conductive network in conductive polymer composites and the use as electroactive multifunctional materials” by Hua Deng [9], “Selective localization of multi-walled carbon nanotubes in thermoplastic elastomer blends: An effective method for tunable resistivity–strain sensing behavior” by , Mizhi Ji [10], and “Effect of nanofiber on material properties of

vapor-grown carbon nanofiber reinforced thermoplastic polyurethane (TPU/CNF) nanocomposites prepared by melt compounding" by Aruna Kumar Barick [11].

As mentioned in Section 1.2, there is strong evidence that the CNF/TPU composite material designed and tested previously had significantly different matrix morphology when injection-molded compared to transfer-molded. When transfer-molded, the neat TPU was significantly more opaque than its injection-molded counterpart, suggesting a higher degree of hard segment association, and pseudo-crystal formation, leading to improved composite conductivity. The authors of "Progress on the morphological control of conductive network in conductive polymer composites and the use as electroactive multifunctional materials" state a similar finding. In the article, the authors emphasize the importance of "morphological control of the conductive networks" in order to obtain desired electrical properties of conductive composites. The authors talk about various potential methods for manufacturing conductive composites, such as melt mixing, and post processing operations that can be utilized to alter the morphology of the polymer matrix, such as thermal annealing. They then go on to elaborate on various methods that can be potentially used to characterize the morphology of the material. Some of the most important ones being Scanning Electron Microscopy (SEM), Wide Angle X-Ray Diffraction (WAXRD/XRD), and Raman Spectroscopy. They advise that SEM images are mostly useful at verifying location and the orientation of fibers within the polymer matrix, while XRD and Raman spectroscopy can be used to determine matrix morphology and matrix orientation. The authors state that it can be very difficult manipulating the morphology of a composite. One suggestion they make to get around that problem is to use various blends of polymers to adjust the interaction of fibers and polymer morphology [9].

Expanding on this idea are the authors of "Selective localization of multi-walled carbon nanotubes in thermoplastic elastomer blends: An effective method for tunable resistivity–strain sensing behavior". In this study, Mizhi Ji and the team look to develop a procedure for customizing the conductive response of a composite material. They accomplish this by using two different thermoplastic elastomers, one of which is a TPU, as a matrix for multi walled carbon nanotubes (MWCNTs). The other polymer used in the study was Poly Styrene Butadiene Styrene (SBS). This polymer was chosen because like TPU, it is a thermoplastic elastomer, however, it has more hard segments. First, using a melt mixer, the authors blended SBS with 4 weight percent MWCTs (SBS-4NT), and then 8 weight percent MWCNTs (SBS-8NT). Similarly, they then go on to mix TPU with both 4 and 8 weight percent MWCNTs, labeled TPU-4NT and TPU-8NT, respectively. Lastly, researchers blended the SBS-8NT with neat TPU, SBS-4NT with TPU-4NT, and TPU-8NT with neat SBS. The new composites that they develop all have varying conductivity strain behaviors, even though each material is made up of the same weight percent MWCNT, SBS, and TPU. In this study, it was found that the SBS-8NT mixed with TPU had the highest initial resistivity, although it also had the highest change in resistivity with applied strain. At the same time, TPU-8NT mixed with SBS had the lowest initial resistivity but did not have as steep a change in resistance as the other materials [10].

Lastly, in "Effect of nanofiber on material properties of vapor-grown carbon nanofiber reinforced thermoplastic polyurethane (TPU/CNF) nanocomposites prepared by melt compounding" the authors perform a comprehensive analysis of electrical, thermal, and mechanical properties of TPU mixed with CNFs at varying weight percentages. The authors examination of the XRD graphs of TPU blended with CNFs was of utmost importance in understanding the interaction between the matrix and filler. In short, the authors found that TPU

generally has an XRD peak around a 2θ of 19.75 degrees. This is said to be related to the hard domains of the TPU and are not shown to be greatly affected by the addition of CNFs, which have an XRD peak around a 2θ of 26 degrees. The location of these peaks remained consistent throughout the XRD tests, with varying amplitudes of reflected X rays detected for the varying weight percentages [11].

These studies, as well as others, help to justify continued research and interest into conductive polymer composites. Specifically, TPE/CNF nanocomposites are of great interest due to the potential for flexible conductors, biomedical valves, and strain sensing applications.

CHAPTER II

TEST METHODS AND EXPERIMENTAL SETUP

2.1 Electrical Resistivity Testing

Electrical resistivity of a material is a measure of how strongly that material resists the flow of electric current. Conversely, the electrical conductivity of a material is a measure of how easily the material allows the flow of electric current. The two material properties are inversely related. The electrical resistivity of a material can be experimentally determined using Equation (1).

$$\rho = R\frac{A}{L} \tag{1}$$

In the equation, ρ is the materials resistivity, R is the samples recorded resistance, A is the sample's cross-sectional area, and L is the length or thickness of the sample. Once a material's resistivity is determined, the resistance of any part made of that material can be determined.

Resistivity testing of the various composite samples was performed on a servo hydraulic material testing System (MTS 810) under a range of compressive loads and sample orientations. The loads were determined by comparing the cross-sectional area of the test specimen and applying a load that would stress the sample to a state within the range of what the actual

AdapterPlus™ steering pad sees in operation. Table 2 provides a list of sample loading scenarios, for the conductive insert.

Table 2. Conductivity test loading conditions

Test Specimen	Prototype Pad			Single Insert	
				Transverse Direction	Longitudinal Direction
Load [lbs]	1550	3550	5550	130	60
Stress [psi]	59	134	210	222	310
Stress [kPa]	405	926	1448	1530	2137

When fully loaded, a standard class F and K class bearing will carry 34,400 pounds (153 kN). The railcar itself accounts for 17% of the total carrying capacity. Meaning, that when the car is unloaded, a bearing will still carry 5,848 pounds (26 kN). This equates to a maximum stress of 1,303 pounds per square inch and a minimum stress of 221 pounds per square inch seen by the top of the steering pad. For the single inserts, all loads chosen in the experiments stress the samples to a state within that range. Previous studies by Basaldua have shown that increasing the compressive load generally has a positive impact on electrical conductivity of the material [3]. Therefore, for the prototype pad, the worst-case scenario for the material conductivity occurs at the lowest stress state. The loads chosen for the prototype pad stress are more stringent than that seen in the field, which accounts for some potential manufacturing deviations.

Two distinct methods were used for applying an electrical charge to the system. For the preliminary injection-molded samples, the voltage was increased until a desired current of 270 milliamps was achieved. This method was used to determine whether the material was suitable for injection-molding into more complex geometries. For the tests thereafter, a constant potential difference of 5, 7.5, 10, 15, 20, and 24 volts was applied across the pad. In this case, various

voltages were used to determine the electrical characteristics of the material for potential alternative applications, as well as to account for any inefficiencies or losses that may be seen in field use.

For all resistivity tests, the samples were isolated from the MTS compression platens using ½" thick polymer sheets. For the prototype pad, a class F bearing cup (often referred to as the outer ring) was cut in half axially, and then welded to a ¼" thick steel plate. This provided a flat surface for the MTS compression platens on one side, as well as a way to mount the bearing adapter assembly on the opposite side. The cup was reinforced by welding half circle supports on the front and rear faces. A potential difference was applied to the system using a sheet of 20-gauge sheet metal on top of the prototype pad, and a bolt drilled into the bearing adapter. The load was then distributed to the top face of the prototype pad using an I-beam. A schematic of the test setup as well as the actual test setup, minus the I-beam, are shown in Figure 7 (left) and Figure 8, respectively. For resistivity testing of the initial pucks, transverse resistivity, and longitudinal resistivity, the voltage was applied to the system via two pieces of sheet metal on top and bottom of the test sample, shown in Figure 7 (right).

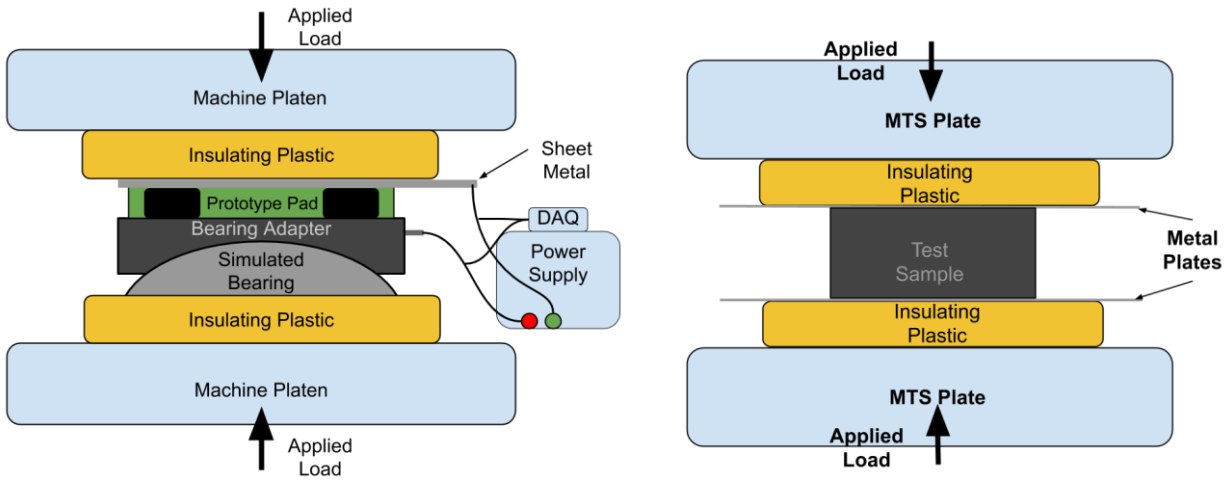

Figure 7. Schematic of electrical conductivity test setup for prototype pad (left), generic conductivity setup (right)

Figure 8. Conductivity test experimental setup

2.1.1 Target Resistivity Determination

Once testing procedures had been developed, a target resistance could be determined. Two different tests were performed to accurately determine the resistance of the valve and the corresponding necessary resistance to achieve actuation. For the first test, an EMCO Resistance Decade Box was placed in series with the air actuator valve and a multimeter, and 24 volts were applied to the system. The setup is shown in Figure 9. Starting at 40 ohms, the resistance of the box was manually decreased by 1 ohm increments until the air valve made an audible click. The voltage, current, and resistance were recorded, and the results are shown in Table 3.

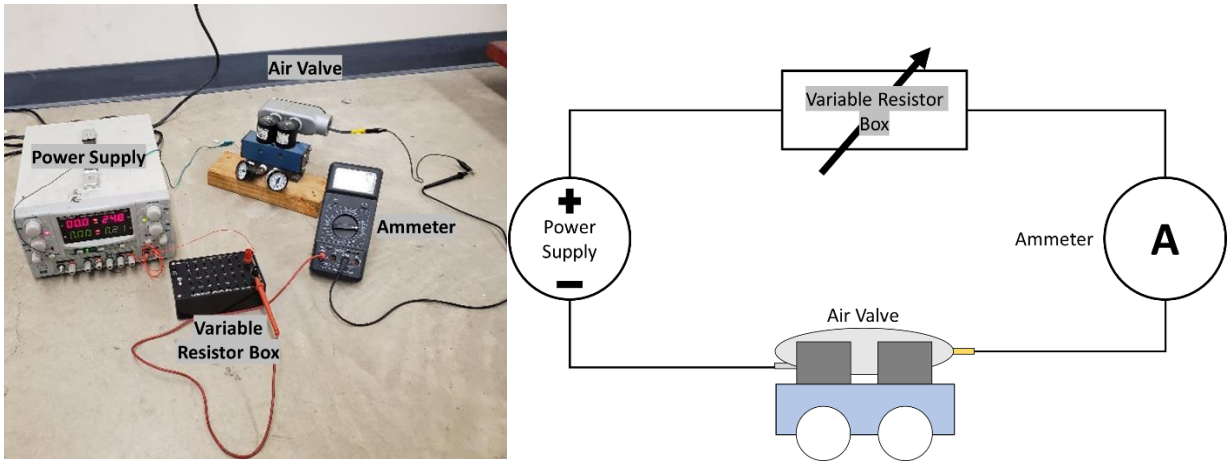

Figure 9. Target resistance determination, method 1. Experimental setup (left), and circuit diagram (right)

Table 3 Target resistance determination

Test #	Voltage [V]	Current [A]	Resistance [Ω]
1	24	0.23	33.10
2	24	0.23	32.00
3	24	0.23	31.10
4	24	0.23	31.10
5	24	0.23	33.00
Average	24	0.23	32.06

From this simple experiment, it could be determined that on average, a resistance of approximately 32 ohms or less is required to actuate the valve when 24 volts are applied to the system.

The alternative method of resistance determination involved placing the air actuation valve in a resistance determination circuit discussed in Section 2.1.2. An initial potential difference of four volts was applied to the system. Then, the applied voltage was slowly increased in 4 volt increments until an audible click was heard, at which point the system was allowed to reach steady state. The setup and corresponding data are shown in Figure 10 and Figure 11, respectively.

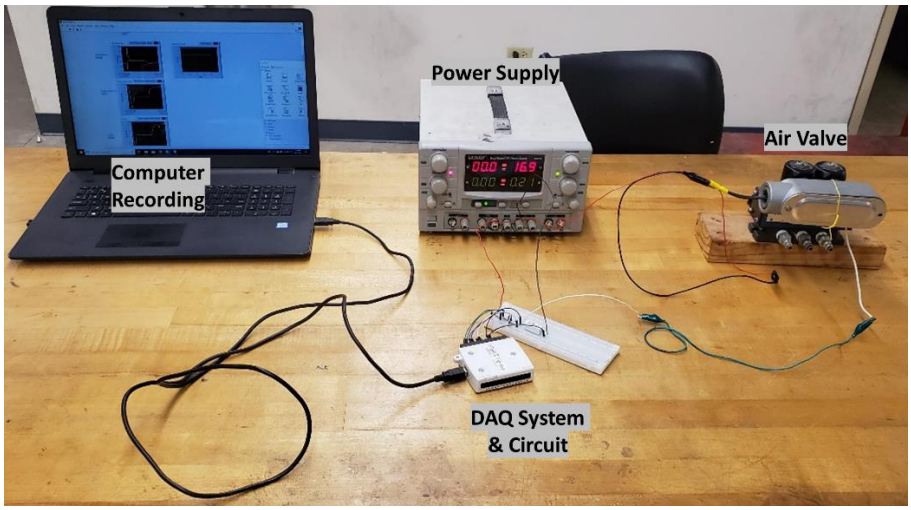

Figure 10. Target resistance determination, method 2

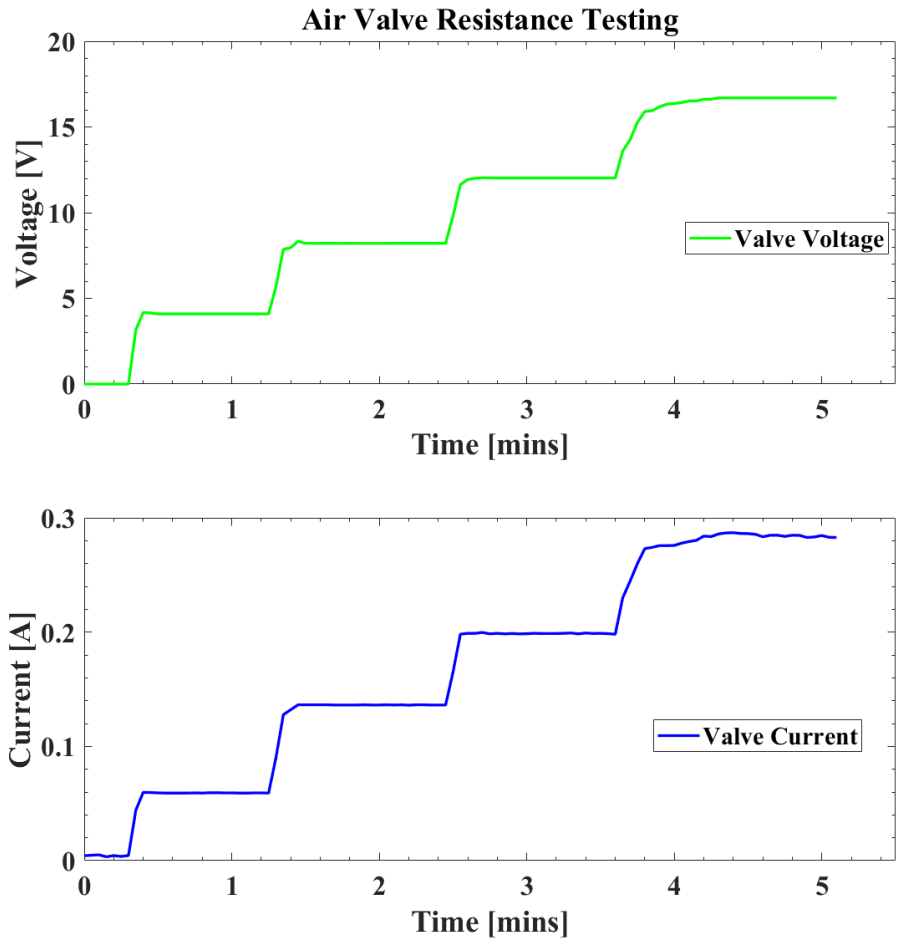

Figure 11. Voltage and current draw of air valve to actuate

Using the data from the experiment, and Kirchhoff's Voltage Law, it was determined that the valve requires approximately 16.05 volts to achieve solo actuation. If 24 volts are typically applied to the system, that leaves a remainder of 7.95 volts potential difference available to the conductive steering pad. Since the conductive pad and the actuation valve are in series, they must share the same current of 0.270 milliamps. Using these two variables and substituting into Ohm's law, it was determined that the necessary resistance of the prototype steering pad must be 29.44 ohms or less for valve actuation. Compared to the initial target resistance of 32 ohms, the two

target resistances agree to within 8 percent. For the experiments, an ideal resistance of 25 ohms was chosen, which allows just over 15 percent variance in resistance measurement. However, the 29.44-ohm resistance determined will also be represented in the figures as the maximum resistance. These resistances will be converted into corresponding resistivities, which depend on the dimensions of the tested samples. In all scenarios, an adequately conductive sample will have a resistivity below the target line. That is to say, that minimal resistivity equates to higher conductivity, which is desirable for valve actuation.

2.1.2 Data Collection Circuit and Measurement Uncertainty

In order to accurately measure the resistance and current flow through the pad, a National Instruments (NI) USB-6008 data acquisition system (DAQ) programmed using LabVIEW^{TM} was used along with a simple circuit that was developed. A schematic of the developed circuit and setup is shown in Figure 12. A large 100 kilo-ohm total resistance was put in parallel with the tested sample to ensure that the majority of the current flows through the sample. The 100 kilo-ohm resistance was broken into three legs of 33 kilo-ohm resistors so that the voltage drop across each resistor was in the allowable measurement range of the DAQ. The shunt resistor is small enough so that it allows the current through the system to be measured with negligible decrease to the voltage across the test sample. Using these values, any unknown resistance can be determined using a combination of Kirchhoff's and Ohm's laws. This setup allowed for continuous measurement of various samples and could detect small fluctuations in resistance over longer periods of testing.

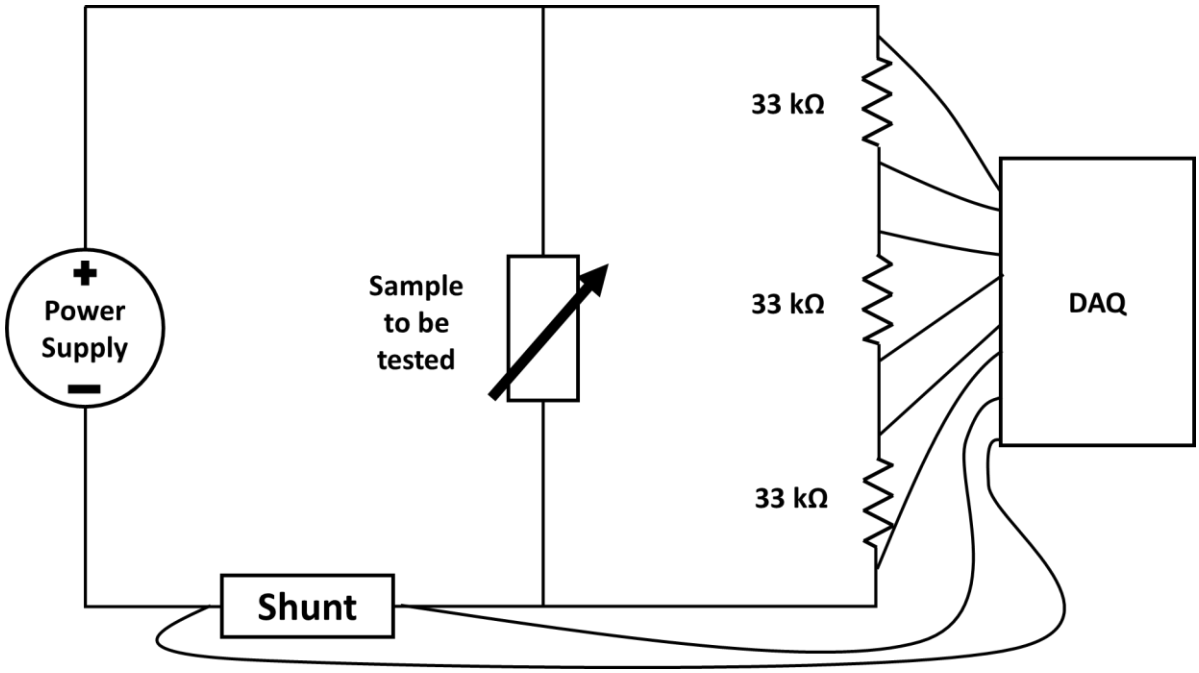

Figure 12. Resistance determination circuit

2.2 X-ray Diffraction (XRD)

X-ray diffraction is a type of X-ray spectroscopy that measures the intensity of a diffracted beam of X-rays to determine characteristics of a material such as crystal structure, chemical analysis, stress measurement, and more [12]. X-rays were first discovered in 1895 by Wilhelm Conrad Roentgen while working with a cathode-ray tube in his lab. He discovered that the rays generated by the tube could pass through many different types of substances but would create a shadow when the beam came into contact with more dense objects, such as metals and bones. Fast forward to 1912, and Max von Laue had discovered that the space lattice structure of a crystalline material was responsible for the interference seen in the X-rays. Two years later, father and son duo, W.H Bragg, and W.L Bragg furthered the ideas by Laue by developing a relationship between the wavelength of the incoming X-rays and the spacing between atomic planes, called Bragg's Law.

The main components of an X-ray diffractometer are the X-ray tube, the sample holder, X-ray detector, and the shielding. The X-ray tube generates a beam of X-rays that is focused on the sample. Then, depending on the lattice structure of the material, and the angle of the incoming X-rays, the scattered rays either constructively interfere or destructively interfere, the magnitude of which is picked up by the detector. In order for constructive interference to occur, the incident angle and reflected angles of the incoming rays must be equal. Therefore, knowing the wavelength of the incoming X-rays, the spacing between atomic planes can be determined using Bragg's law.

$$n\lambda = 2dsin\theta \quad (2)$$

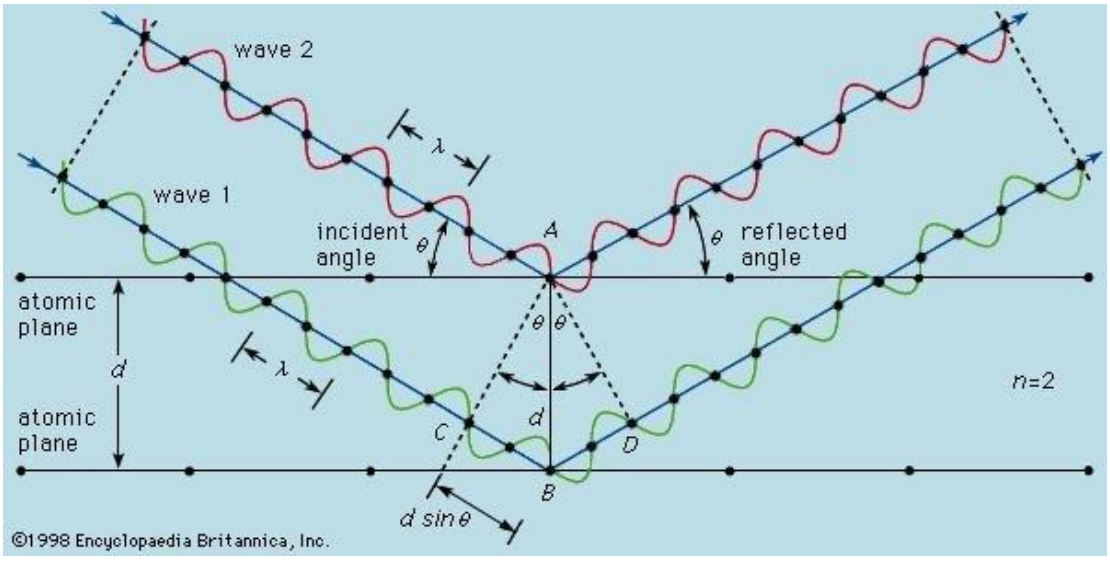

Figure 13. Visual representation of X-ray diffraction following Bragg's law [13]

For these experiments, X-ray diffraction was used to compare the crystal structure of TPU and TPUCNF composites manufactured via transfer-molding and injection-molding. From the spectrums, a hypothesis of how the differing pseudo-crystals affect carbon nanofiber networks and the resulting conductivity can be made.

2.3 Scanning Electron Microscope (SEM)

The Scanning Electron Microscope, commonly referred to by its initial's "SEM", is used to obtain detailed, magnified images of small-scale samples. These samples can range anywhere from 1 cm to 5 microns in width. The SEM has a magnification scope between 20x to 30,000x, with a spatial resolution of around 10 nm. The high-power capabilities of the SEM allow for the production of imagery that provide information on sample surface topography as well as sample composition.

A scanning electron microscope is composed of an electron source, a series of electron lenses, electron detectors, and a computer. The basic configuration is pictured in Figure 14.

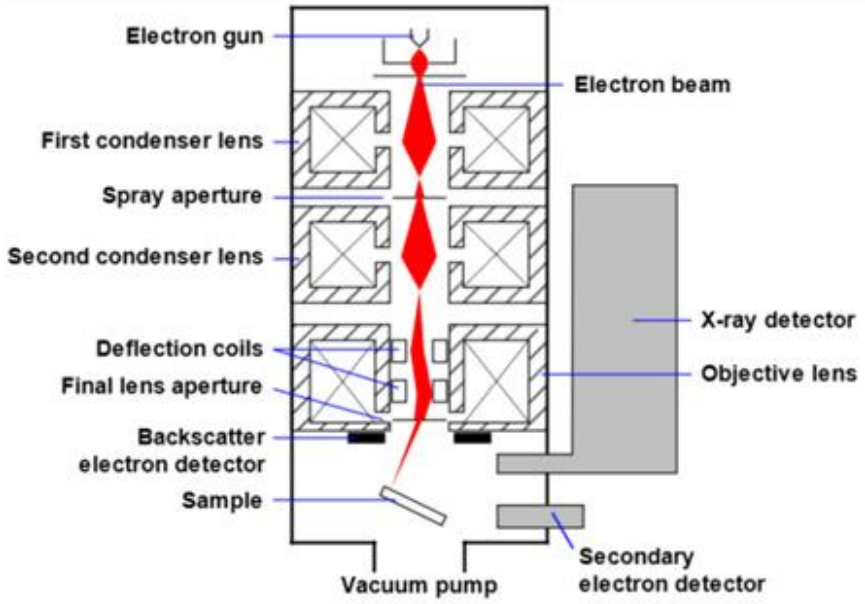

Figure 14: Schematic for scanning electron microscope [14]

As the name suggests, the SEM uses a beam of electrons generated by an electron gun accelerated and focused on the sample using a series of lenses. The electrons collide and interact with the atoms that compose the sample creating secondary and backscattered electrons. These

two types of electrons are the most common signals used to form SEM images. This beam/sample interaction can be seen in Figure 15.

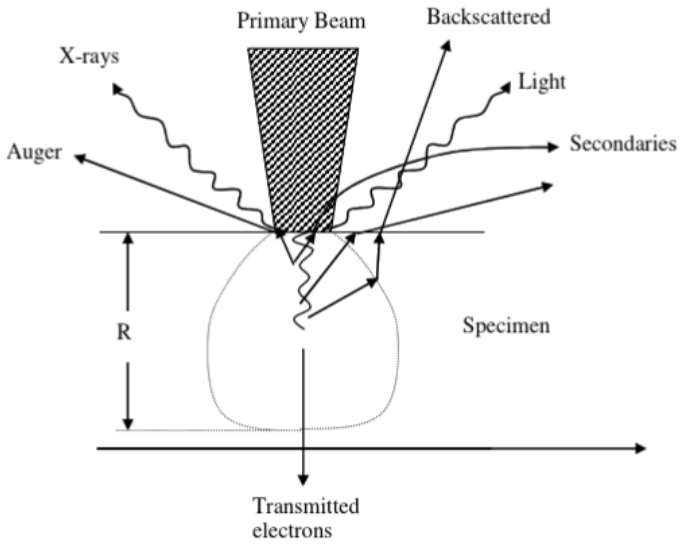

Figure 15: Electron beam interaction with test sample [14]

Secondary electrons are produced via inelastic collisions near the surface of a sample. These electrons have relatively low energies, typically between 0.5 eV to 5 eV but up to 50 eV. Backscattered electrons are created by elastic collisions from deeper levels within the sample. These electrons have energy greater than 50 eV up to the beam energy. Occasionally, electrons from lower orbitals are dislodged from the sample. These electrons are called Auger electrons. The energies of these electrons can be observed as characteristic peaks in the energy spectrum and give some insight into the chemical composition of the sample [15].

In order to prepare a sample for SEM imaging, the sample must occasionally be coated in a thin layer of gold, silver, or another type of conductive material via sputter coating. The conductive layer helps to attract the electron beam to the sample by grounding it. Without this conductive layer, electrons can build up on the surface of the test sample. The built-up electrons then repeal the electron beam and create blurry and pour quality images. If the sample is metal or

moderately conductive, sputter coating is not necessary. In the case of the CNF/TPU composite, the sample was adequately conductive to not sputter coat. Next, the sample is placed in the test chamber. The test chamber is then vacuumed to evacuate any air or dust particles that may interfere with the beam of electrons. Finally, the samples are moved into place, and the electron gun is turned on. The computer is then used to decipher the signals received by the electron detectors and the SEM image is displayed.

Although typical use of the SEM involves imaging the surface of the sample, there is other information and insight that can be obtained by the SEM. For example, the elemental composition of the sample can be obtained via Energy Dispersive Spectroscopy (EDS). This technique involves monitoring the emitted photons generated by the electrons of the sample that are in the X-ray range.

For this analysis, the SEM will be used to verify the dispersion, the length, orientation, and the overall interaction of the TPU and carbon nanofibers within the injection molded samples. Samples were scored with a saw, along the areas of interest, then soaked in liquid nitrogen for 10 minutes. The samples were then removed, wrapped in tissue paper and put in a bag. The contained sample was then hit with a mallet to fracture. The sample was then removed, cleaned with isopropyl alcohol and a microfiber cloth before imaging in the SEM.

2.4 Differential Scanning Calorimetry (DSC)

Differential Scanning Calorimetry (DSC) is a thermo-analytical technique that measures the amount of heat flow, either absorbed or generated, by a sample as it undergoes various thermal transitions [16]. It does this by comparing the amount of heat required to raise the temperature of the sample to the amount of heat required to raise the temperature of an aluminum reference pan and plotting the curve as a function of temperature. For polymers, the measured

heat flow gives insight into the glass transition and melting temperatures, degree of crystallinity, heat capacity, heat of fusion, and more. A schematic on the basic function and operation of the DSC is shown in Figure 16

In this study, the DSC was used to analyze the polymer morphology of injection-molded neat TPU, as well as injection molded composite CNF/TPU and determine the effects of the additional CNFs in the molding process. Also, comparisons between injection molded samples and transfer-molded samples are made in an attempt to better understand how the different processing methods effect the conductivity of the nanocomposite.

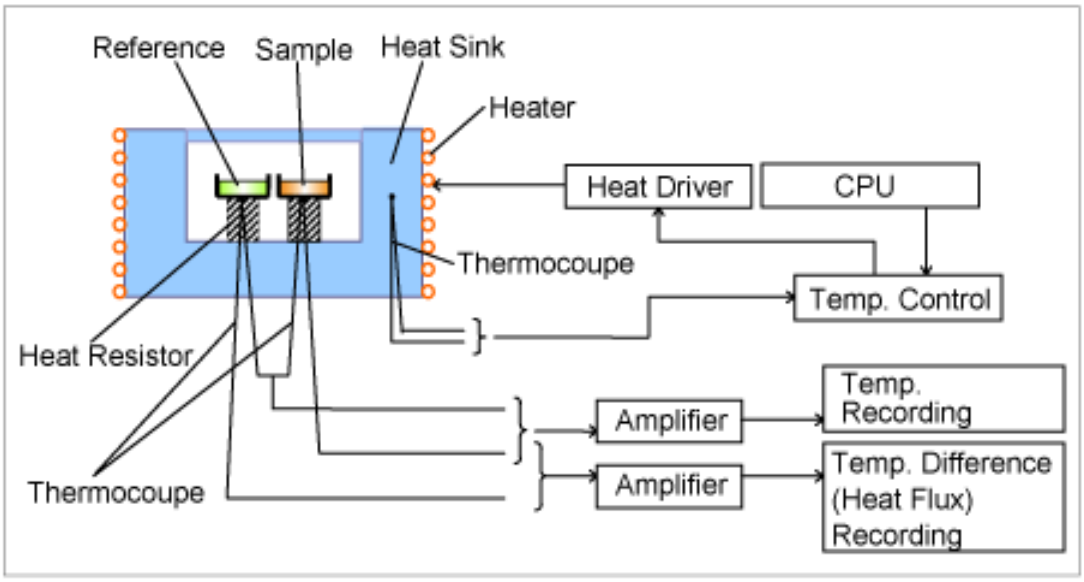

Figure 16. DSC block diagram [16]

A double run DSC was utilized to better understand the effects of the processing methods on the morphology of the material. In these tests, the material was heated at 2°C per minute until 250°C. This heating rate gives an accurate response and minimizes noise, while the final temperature is just under the degradation range, 275°C to 300°C, of the TPU. The material was then held at 250°C for 5 minutes to ensure the entirety of the sample reached a uniform

temperature and that any phase transitions had adequate time to be completed. Then the material was cooled at a rate of 5°C per minute until it reached 60°C, at which point the sample was again re-heated at 2°C per minute until 250°C.

CHAPTER III

PRELIMINARY INJECTION-MOLDED SAMPLES AND PROTOTYPE STEERING PAD DEVELOPMENT

3.1 Injection-molding Setup

The polymer used in this study was a modified Elastollan 1195a donated by BASF. This material had slightly altered hard segments that have a greater affinity for each other, although the full details of the modifications were not disclosed. The material was compounded with Pyrograf® III PR-19-HHT carbon nanofibers by Applied Sciences, Inc[1]. As mentioned in Section 1.2, previous injection-molded carbon nanofiber/TPU composite material was not electrically conductive, so an initial investigation was performed on the new material in order to determine the viability of this new composite for injection molding conductive parts.

The material was first dried in an oven for four hours at 110°C to remove any moisture. Test pucks were then injection-molded using a Boy 22A injection molding machine, with molding temperatures near the highest recommended range to minimize shear stresses in the melt to reduce the risk of fiber breakage. High molding temperatures are also hypothesized to be critical to the full development of pseudo-crystals in the TPU which maximize conductivity. The nozzle of the injection-molding machine was set to 227°C and the remaining four zones were set to 204°C. The injection-molded parts were held in the mold for 90 seconds before being

[1] Applied Science, Inc Phone: (937)766-2020 website: http://apsci.com/

removed and allowed to cool to room temperature. The injection-molding parameters are summarized in Table 4 and

Table 5.

Table 4. Injection-molding temperature parameters

Temperature Parameters					
Mold Temp [°C]	**Nozzle Temperature [°C]**	**Barrel 1 [°C]**	**Barrel 2 [°C]**	**Barrel 3 [°C]**	**Barrel 4 [°C]**
49	227	204	204	204	204

Table 5. Injection-molding parameters

Molding Parameters						
Shot Size [mm]	**Shot hold [s]**	**Mold Hold [s]**	**Total Cycle [s]**	**Injection Speed [mm/s]**	**Mold Clamping Force [N]**	**Injection Pressure (kPa)**
38.5	10	90	100	55	890	13.8

3.2 Sample Puck Conductivity Testing Results

In total, 15 sample pucks were injection molded. The first four pucks were discarded due to potential impurity from residual material in the barrel from previous use of the machine. The final injection molded pucks had an area of 19.4 cm^2, and a thickness of 0.66 cm. The samples were allowed to rest for 24 hours before subjected to the conductivity testing discussed in Section 2.1. Three pucks with the fewest imperfections were conductivity tested. The results are provided in Figure 17. The resistivities corresponding to the ideal 25-ohm resistance, as well as the maximum 29.4-ohm resistance, respectively, are plotted in the figure for reference.

From the figure, it is apparent that at the 1500 kPa stress state, the samples maintained a resistivity that is below the maximum value which permits valve actuation. Meaning that all three pucks are conductive enough to actuate the valve at a stress of 1500 kPa or higher. It is also worth noting that the voltage necessary to achieve these resistances was in almost every instance

less than the 7.5 volts, determined in Section 2.1.1, which is available for the pad. Section 4.1 will discuss why this is important.

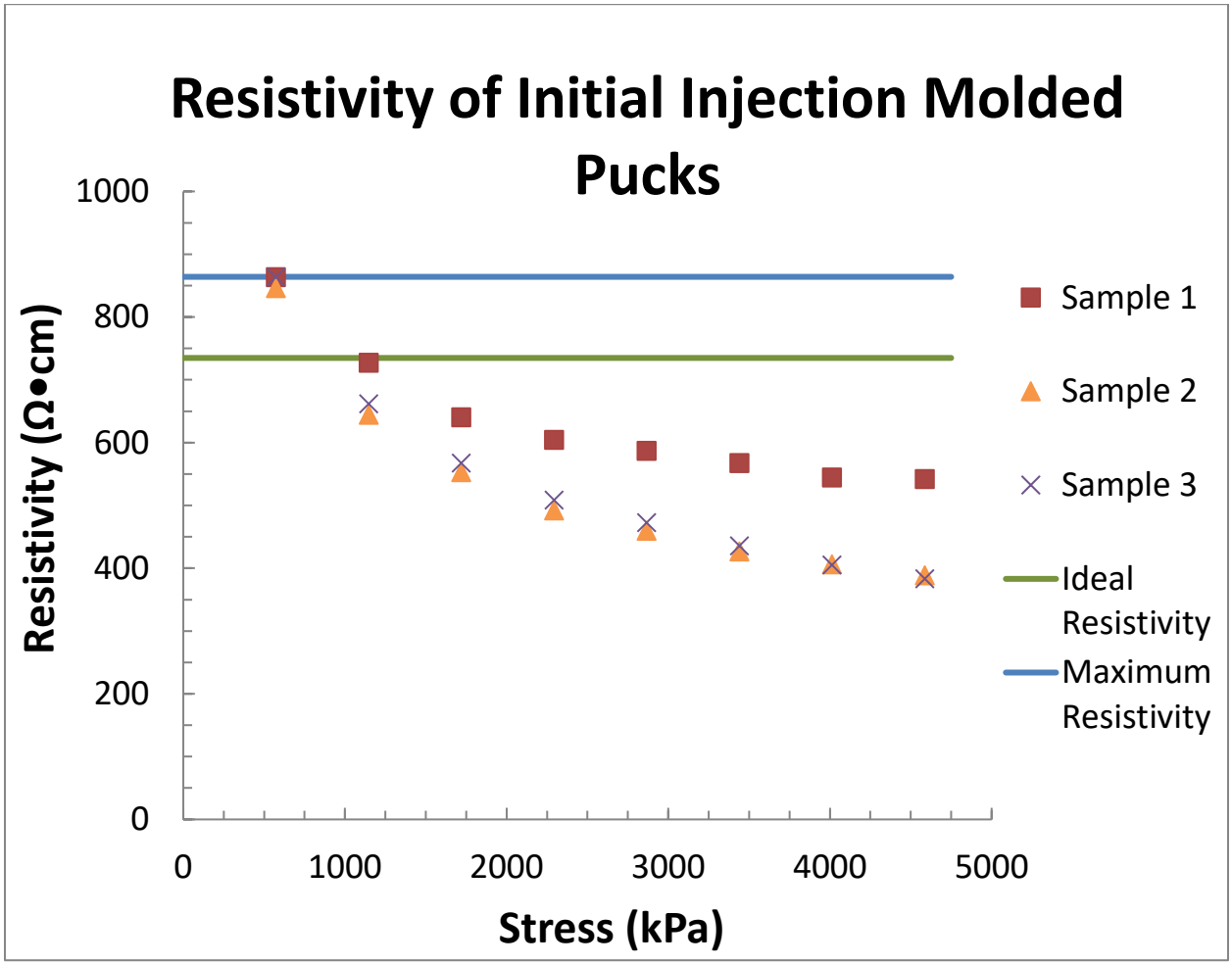

Figure 17. Conductivity testing of initial injection-molded pucks

3.3 Mold Design

After it was determined that the new modified material could be adequately conductive when injection molded, an insert could be designed to incorporate into the steering pad. From previous tests, it is known that maintaining load on the conductive composite is crucial for maintaining adequate conductivity. Figure 18 presents the results of a pressure film study performed by the UTCRS in 2012 [17]. This study determined that the portion of the steering

pad that carries most of the load when the railcar is unloaded was at the interlocks, which are represented by the dark red regions in the image. For this reason, it was decided to create the conductive inserts with the same profile as the interlocks to ensure that the conductive portion of the prototype pad was constantly under load.

Figure 18. Pressure film from 2012 load study [17]

Using a UTCRS computer model of the steering pad, a profile of the interlocks was acquired by taking a section view of the model shown in Figure 19. The mold was created by taking this profile and superimposing it over a cylinder of the same diameter and thickness as an existing mold cavity that was used as a frame to hold the new mold. The idea was to then bond the small inserts together side by side to create a part large enough to achieve sufficient electrical conductivity.

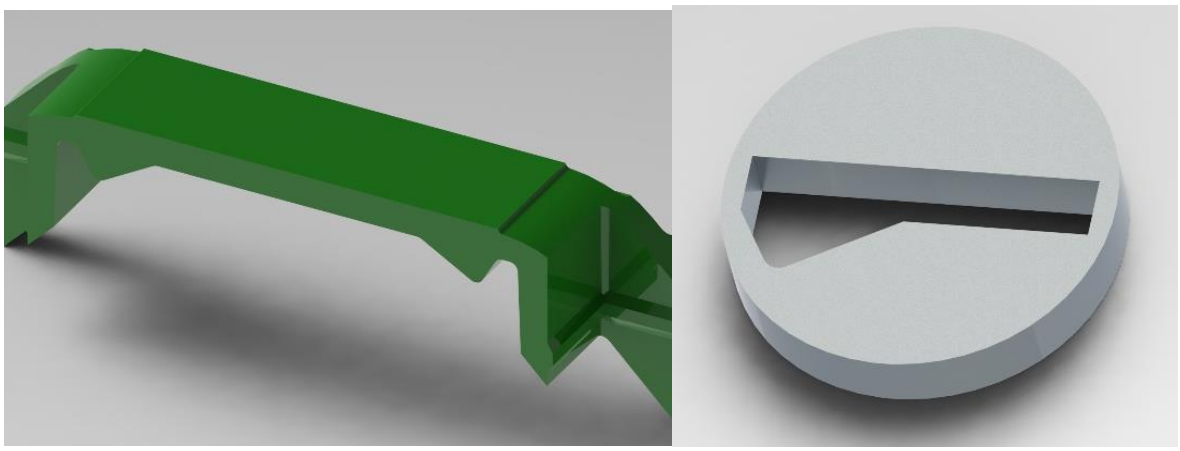

Figure 19. Steering pad section view (left), and injection-mold insert

3.4 Finite Element Analysis: Mold Flow Simulation and Mechanical Analysis

Validation by way of finite element analysis of this design was done using Autodesk Simulation Moldflow to determine problematic areas when injection molding, and Solidworks Simulation to determine how the pad with new inserts would act under stress.

The mold flow analysis hoped to answer three questions: “Will the mold fill? Will the part warp? What orientation will the carbon nanofibers in the parts have?” The simulation was performed using both neat Elastollan 1195a for the fill properties, as well as Estaloc 59300 with 30% glass fiber for the fiber orientation analysis. Estaloc was chosen as it was the only fiber reinforced material in the system library which had molding parameters comparable to Elastollan. The results of the simulation are shown in Figure 20 and Figure 21.

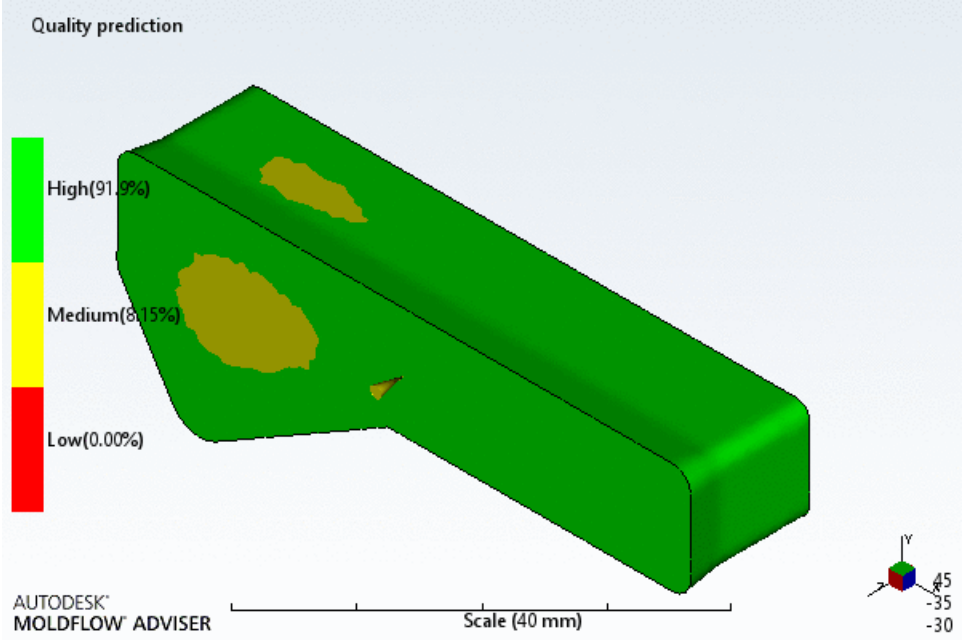

Figure 20. Injection-molded insert areas of potential warping

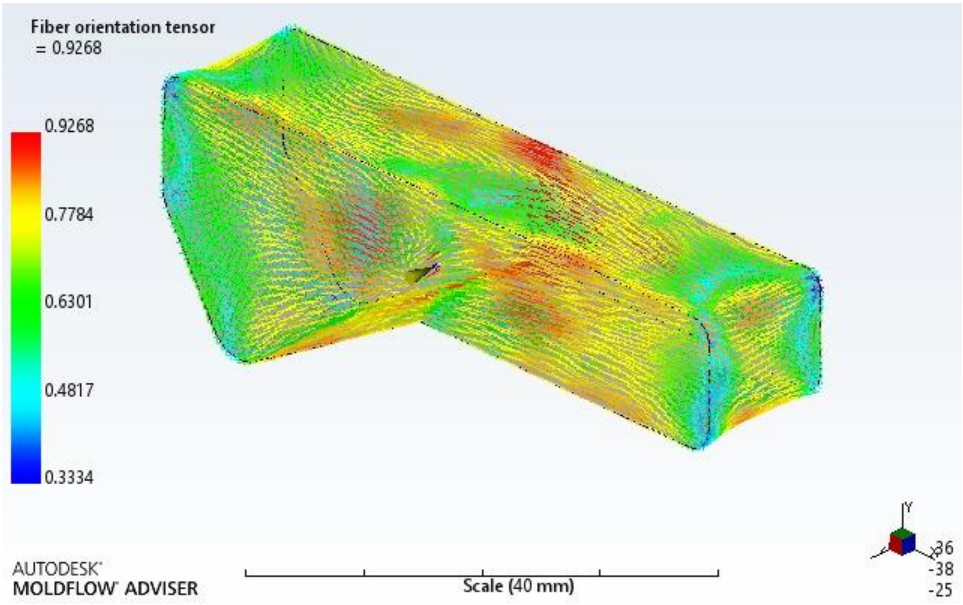

Figure 21. Injection-molded insert fiber orientation analysis

As expected, the portion of the insert that may potentially warp or not properly fill is the thickest portion at the interlocks, although the analysis still determines a fairly respectable 81.1 percent chance of molding correctly. This is likely to improve even more as carbon nanofibers

have been shown to lock polymers in place and prevent excessive shrinkage or warping during molding. Regarding the fiber orientation analysis, the fibers in the middle of the part tend to align in the longitudinal direction, while the fibers at the edges of the insert tend to have a more random orientation. At the surface of the interlocks, the fibers are oriented parallel to the plane of the interlocks. However, towards middle of the interlocks, the fibers are slightly more vertically aligned. It is important to keep in mind fiber orientation of the part because carbon nanofibers are more conductive in the axial direction than they are in the radial direction. In industrial applications, the location of the gate may be modified to optimize the fiber orientation in the insert. However, for this study, due to limitations of the available tooling, the gate location was limited to the front face of the insert.

Figure 22 and Figure 23 show the results of the mechanical analysis performed using Solidworks Simulation. The parameters of the analysis are shown in Table 6.

Table 6. Mechanical finite element parameters

Part	**Material**
Bearing Adapter	Plain Carbon Steel
Adapter Pad Plus Steering Pad	Elastollan 1195a
Injection Molded Inserts	Modified 1195a w/ CNFs
Mesh Information	
Number of Elements	72579
Number of Nodes	118284
Boundary Conditions	
Bearing Adapter	Fixed on Axle
Contact Type	No Penetration
Load	34,400 compressive evenly distributed

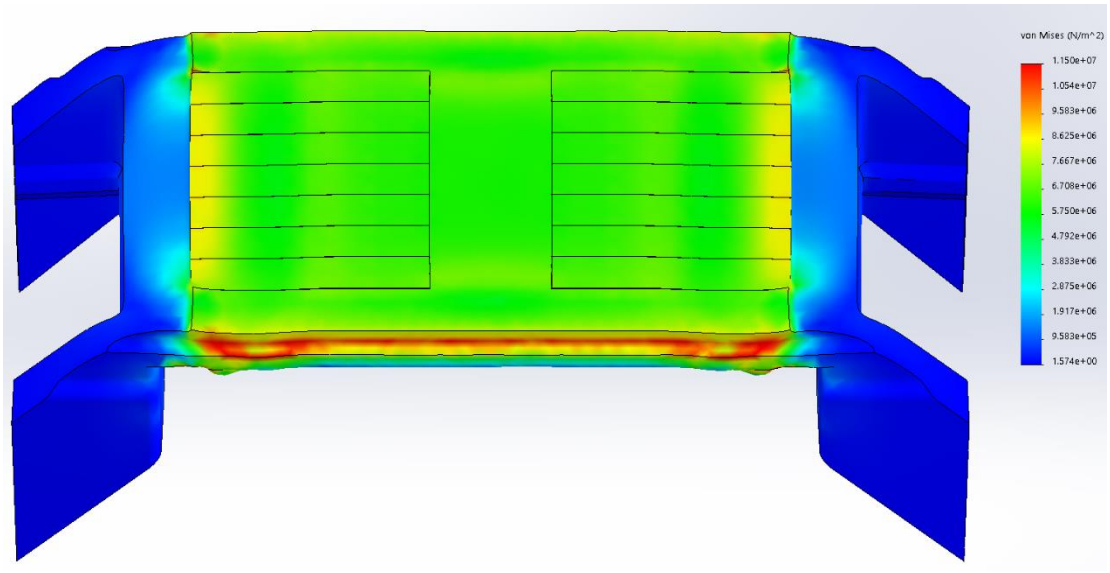

Figure 22. Finite element analysis of prototype steering pad with conductive inserts

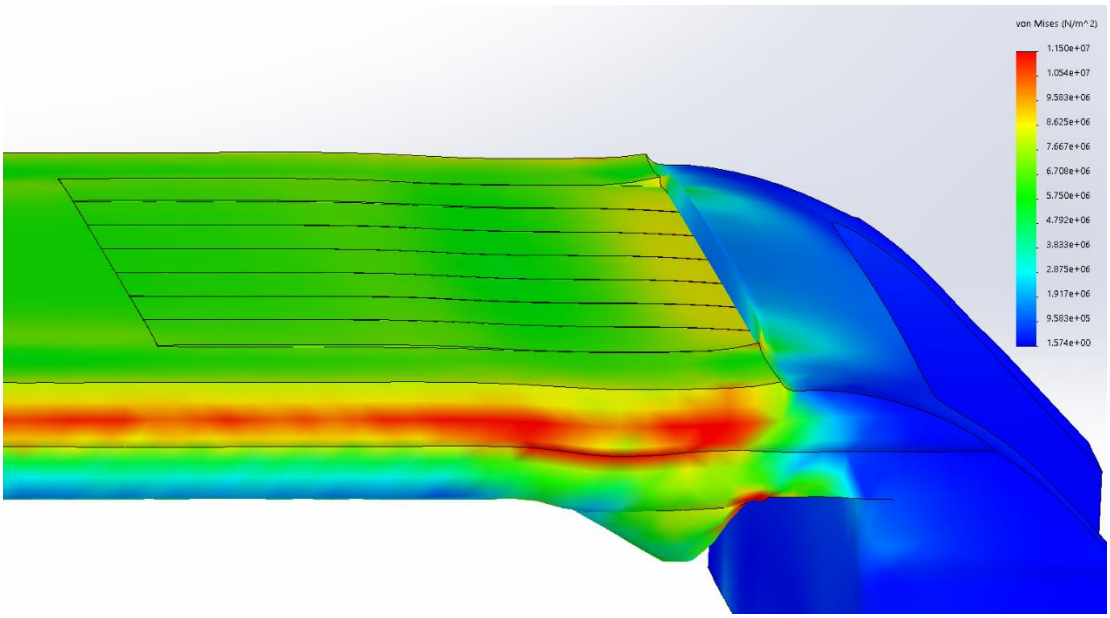

Figure 23. Peel stress at edge

This analysis is a rough estimate of the effects of the insert on the integrity of the rest of the steering pad. It was a “sanity check” on the idea of implementing an insert into the pad in a safe and productive way. Some of the simplifications include the evenly distributed 34,400-pound load across the top of the pad, and the fixed condition of the bearing adapter, not pictured.

However, from Figure 23, the largest stresses of about 10,500 kPa occur at the filleted edge of the pad and up to ½ inch towards the center. Beyond this area, the pad and insert have enough constraining material to essentially be considered under plane strain. There is a slight peel stress at the edges where the pad meets the insert, however, the deformations are minimal, and overall, the integrity of the pad is maintained.

3.5 Mold Manufacturing

Once the design of the mold was complete, manufacturing could begin. During this step, it was important to balance both quality of mold and cost of the mold. Two different methods of mold manufacturing were explored.

3.5.1 3-D Printed Epoxy Mold

For this mold, a 3D-printed part was made that had the desired insert shape in the center of a ½ inch thick 4 inch diameter “cup”. The cup was then filled with Fibre Glast 2000 epoxy resin, stirring constantly, while heating the surface of the resin to remove any air bubbles in the pour. The resin was then allowed to cure for two full days. Once cured, the 3D-printed portions of the mold were removed. The final step was to press the epoxy mold into the mold frame. However, the epoxy mold was brittle and slightly oversized, and fractured while pressing it into the mold frame. The epoxy molds are shown in Figure 24. Although the molds made in this manner were extremely cheap, they required long curing times, many post processing techniques, and maintained rough surface finishes from the 3D-printed material. Ultimately, it was determined that the cost saving by manufacturing the mold in this manner did not outweigh the poor surface finish, and that this was not the optimum method of manufacturing the mold.

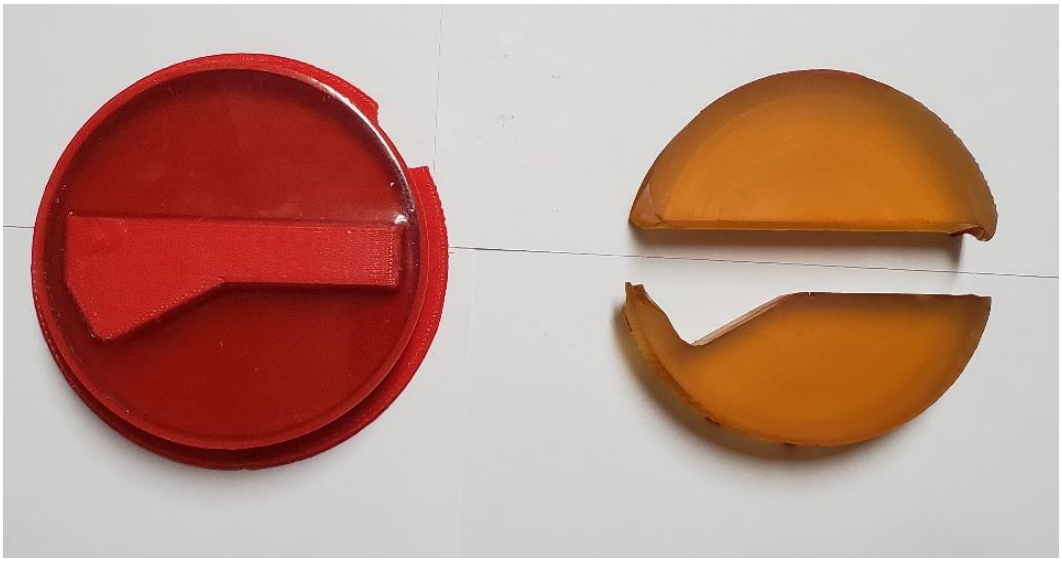

Figure 24. 3D-printed epoxy molds with 3D-printed cup (left) and fractured part after pressing it into mold frame (right)

3.5.2 CNC Aluminum Mold

It was determined that the most effective way to make the mold would be via computer numerical controlled (CNC) mill. To do this, a 4.25-inch diameter rod of raw aluminum stock was machined to 3.996-inch diameter in the lathe and faced to the necessary ½ inch thickness. Next, two holes were drilled and tapped in the piece so that it could be mounted in the CNC mill. Lastly, the piece was centered in the CNC, and the desired shape was milled into the part. The part was then removed and pressed into the necessary frame for molding. The final machined mold is shown in Figure 25. Compared to the previous mold manufacturing method, this method

required nearly the same amount of preparatory work, minimal post processing, faster manufacturing times and had a great surface finish.

Figure 25. CNC aluminum mold

3.5.3 Mold Fame Modification

In order to manufacture quality parts, and to simulate actual manufacturing conditions, modifications to an existing mold housing had to be made. Five holes, two on the top, two on the side, and one on the bottom, were drilled and tapped to allow for the circulation of heated water in order to maintain the mold at 40°C, required by the current steering pad manufacturer. The CNC-manufactured aluminum mold was then pressed into the housing using a manual hydraulic press. Once the mold was pressed into the frame, eight gates were milled across the face of the assembly. These gates provide an escape for any air in the mold to be removed, as well as to allow a small amount of flashing to ensure the part is completely packed and filled, and to minimize shrinking or any other defects. The completed mold is shown in Figure 26.

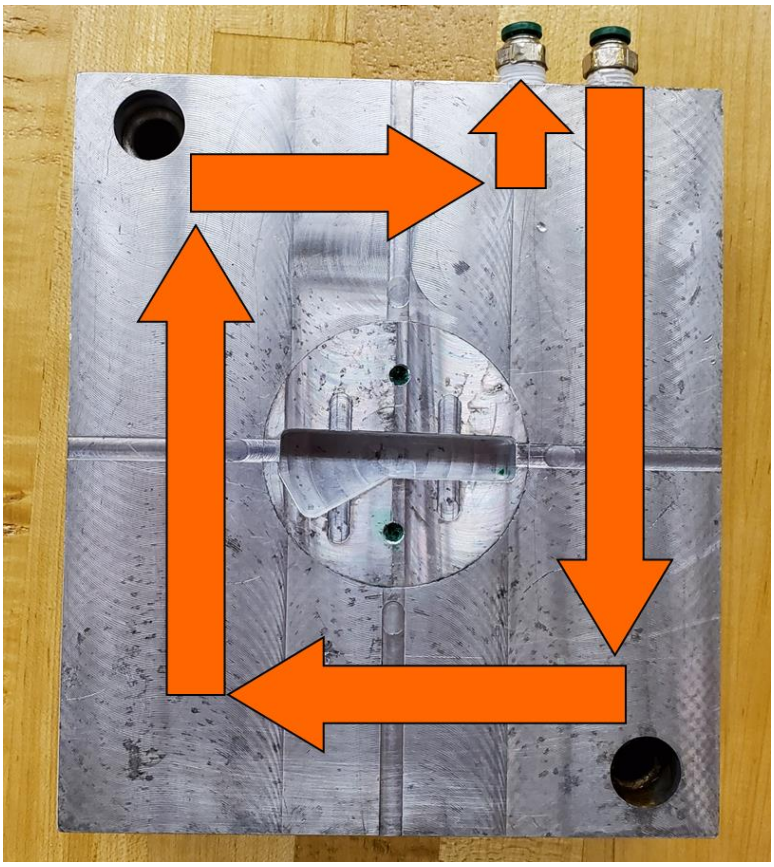

Figure 26. Completed mold with hot water circulation layout

3.6 Injection-molding Prototype Pad

Prior to molding, the composite material was dried in an oven for four hours at 110°C to ensure parts were free of moisture and to minimize defects. Again, the inserts were made using a Boy 22A injection molding machine using the parameters discussed in Section 3.1, Table 4, and Table 5. The mold was held at a constant 40°C throughout the molding process by means of a heated water circulation system.

After molding the parts, they were allowed to rest for 24 hours and were then epoxied together with a polyurethane compatible adhesive (JB Plastic Bonder) and bonded side by side. The bonding was done primarily to facilitate handling and installation of the parts and does not provide any additional structural integrity during pad loading. Throughout the curing phase,

excess squeezed out adhesive was scraped off the top and bottom surfaces of the inserts to ensure that adhesive did not interfere with the conductivity of the parts. The assembled insert prototype is pictured in Figure 27. The relevant section of a standard TPU pad was removed by milling and the assembled inserts were then bonded into the pad. The final prototype pad with conductive inserts is pictured in Figure 28.

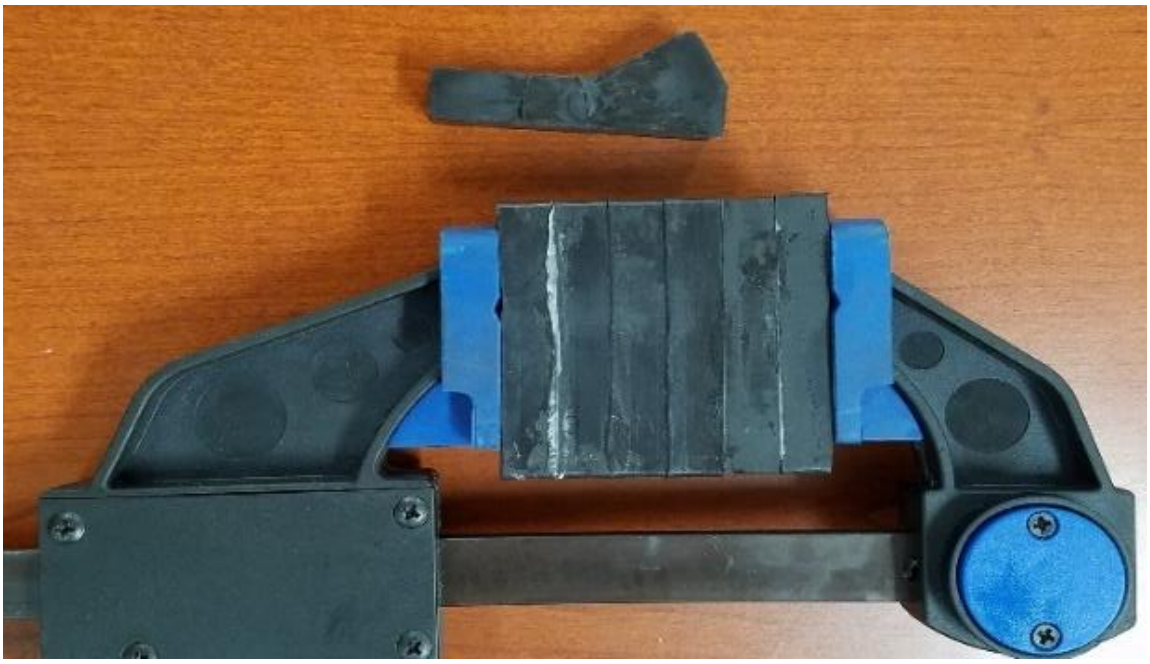

Figure 27. Injection-molded inserts epoxied together

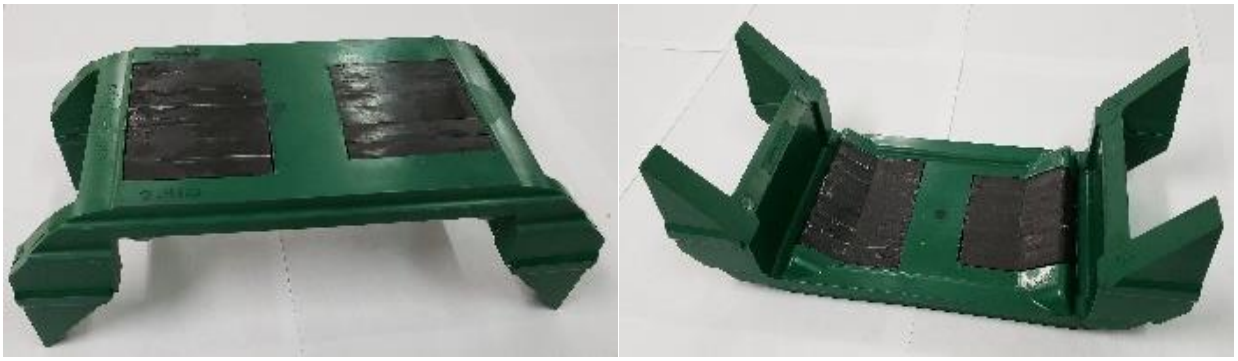

Figure 28. Conductive insert pressed into AdapterPlus™ steering pad

CHAPTER IV

RESULTS

The following section outlines the results of the various tests discussed in Chapter III used to characterize and understand the behavior of the conductive composite material. The results for any additional tests performed can be found in the appendices. However, the ones presented and explained in the main body of this thesis are considered to be the most pertinent.

4.1 Electrical Conductivity

The prototype conductive pad is composed of two individual assemblies of seven inserts each. The combined area of the two inserts was 94.19 cm^2, with an average thickness of 3.648 cm. The recorded resistivity was determined by substituting the recorded resistance from the measurement system, along with the area and thickness values into Eq (1). The resulting values were then plotted in the figures. The two parameters explored in these experiments were the effect of load and voltage on material resistivity. In general, the shape of the graphs remains consistent throughout various loading and voltage scenarios. Like any system, the response of the prototype pad can be broken into its transient and steady state response. For the particular application of valve actuation, the steady state response is most important, due to the fact that once the bearing assembly is put into service, it is not removed, and the steering pad is under load for the rest of its operating life. It is however interesting to examine the transient response for other potential applications.

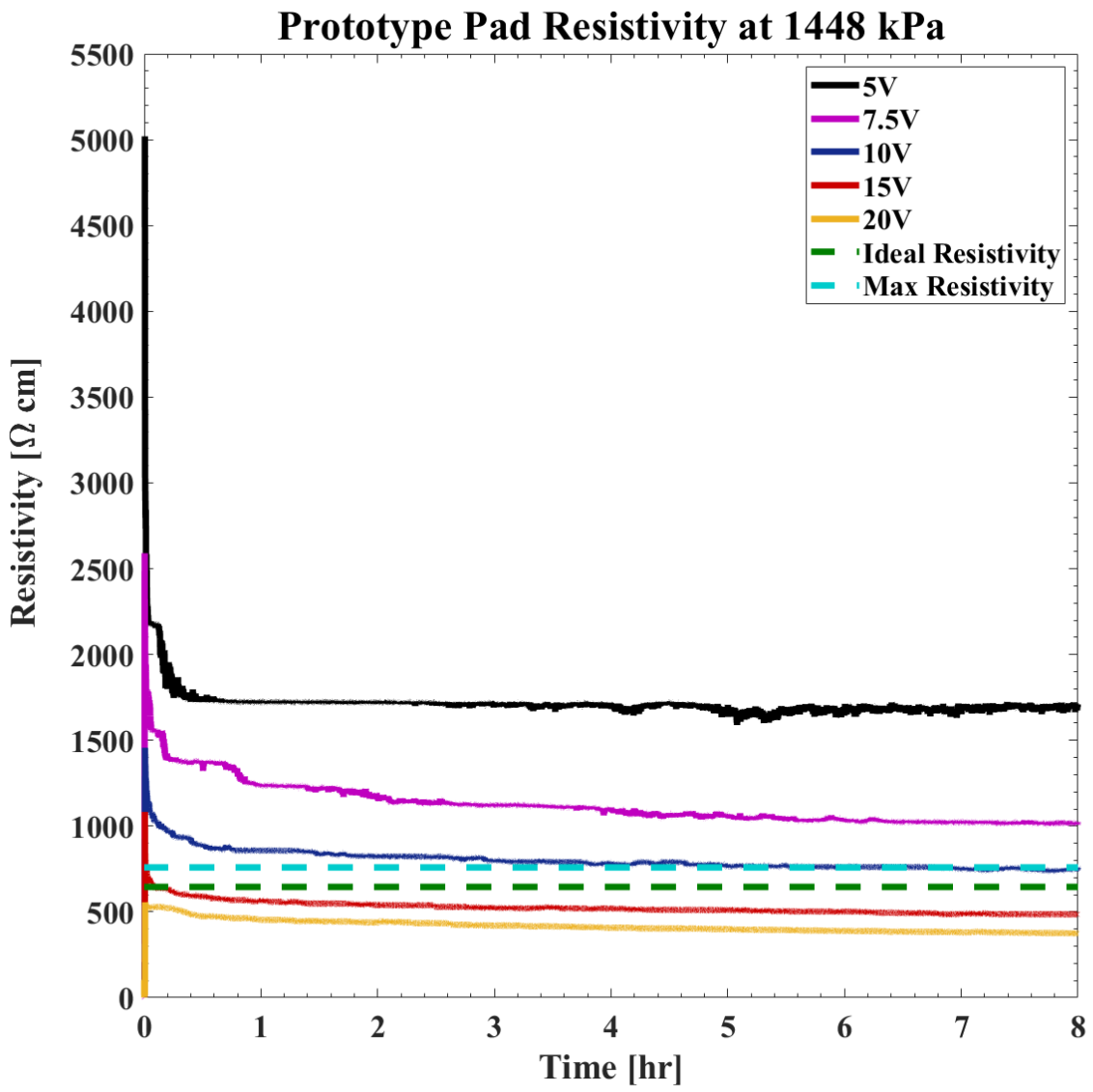

Figure 29. Prototype conductive pad resistivity at 1448 kPa applied stress and various applied voltages

Figure 29 shows the effect that voltage has on material resistivity at 1448 kPa applied stress. Recall that this stress corresponds to the minimum stress seen by the steering pad in normal operation. It can be seen that as the voltage increases, the resistivity of the material decreases at a decreasing rate. This means that as the applied voltage increases, the magnitude of these changes slightly diminishes. This is due to the potential well phenomenon discussed in

section 1.4. In short, by increasing the applied potential to the system, the electrons traveling along the nanofiber networks have increased energy that enables them to tunnel over greater distances or barriers. Also, worth noting is the resistivity of the material at an applied potential difference of 7.5 volts. From section 2.1.1, it was determined that the pad has approximately 8 volts available to it when in series with the 24-volt supply and air valve. This means that for the valve to actuate in operation, it requires a resistivity at 8 volts below the plotted "Target Resistivity" line. However, the figure does show that the pad could potentially actuate the valve if the available voltage to the pad could increase to approximately 12 volts. This would be possible if the voltage of the supply was increased, or if the resistance of the valve was decreased.

Figure 30 explores the effect that load has on conductivity of the prototype pad. The overall response is similar to that seen in Figure 29. Naturally, as the applied stress, and corresponding strain, increases, the sample's resistivity decreases, or conversely the conductivity improves. This is due to the carbon nanofiber network physically moving closer together as the material is compressed. As this happens, the fiber networks develop more active branches as portions of fiber networks that were once separated either touch or become close enough to allow tunneling of electrons. Again, the effect of additional stress on the resistivity declines because there are a finite number of fiber networks that can be active within the composite and once those are all active, further reduction of fiber spacing does not yield significant improvements in conductivity. Furthermore, excessive loading has the potential to have a negative impact on the conductivity of the composite material. If the composite is loaded beyond its yield point, cracks may form that disrupt the conductive nanofiber networks within the matrix. Ultimately, the cracks would create voids and increase the distance between fiber networks, decreasing the

number of active chains and decreasing composite conductivity. This particular phenomenon was not explored in these experiments, as all tests performed were well within the allowable stress range of the composite material, however it is worth noting.

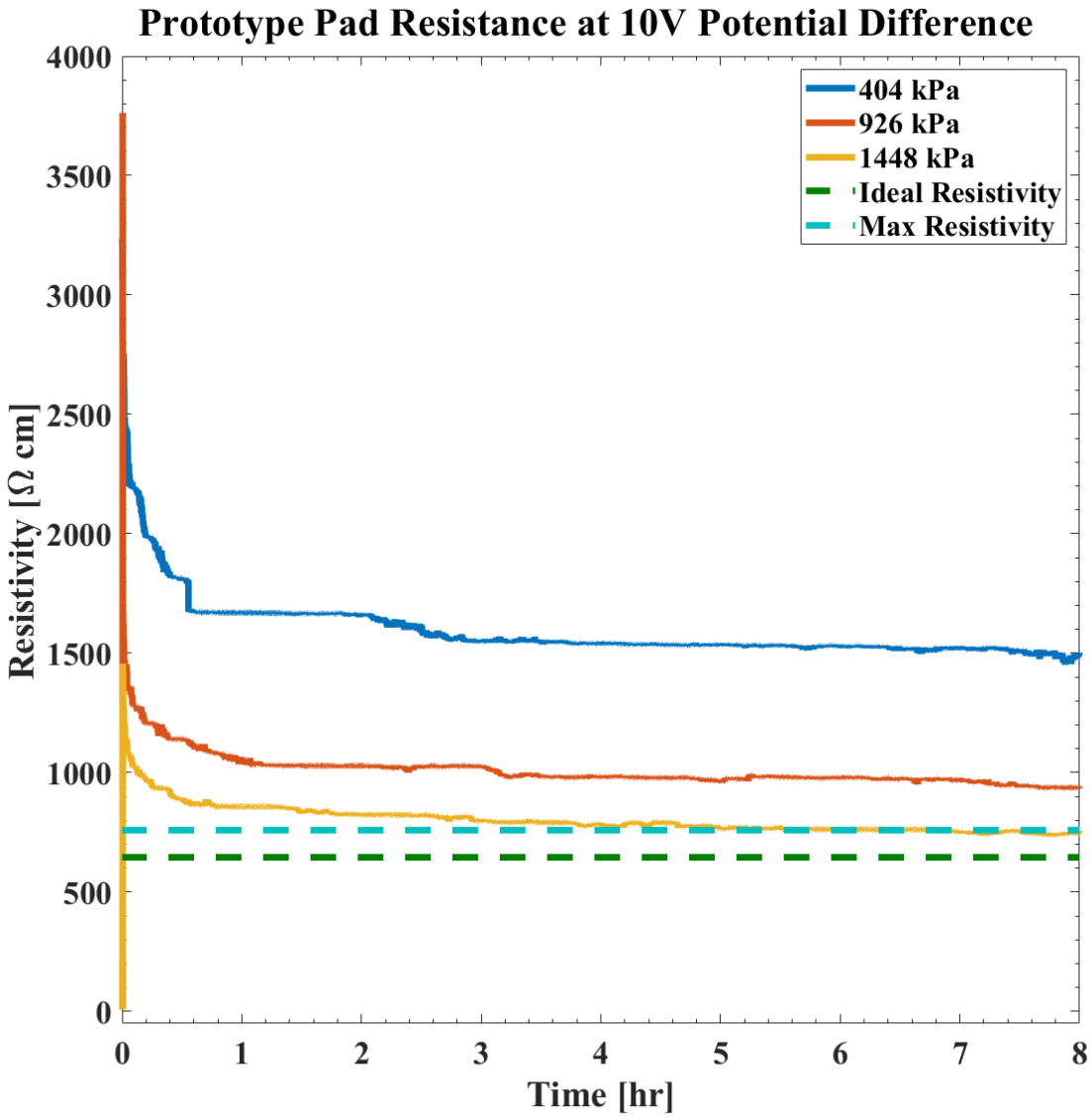

Figure 30. The effect of stress on prototype conductive pad resistivity at 10-volt potential difference

4.1.1 Transient Response

As previously mentioned, the transient response is not as important for the function of the prototype steering pad, however, it may prove to be a critical characteristic if the material is to be adapted for other applications such as an onboard load sensor. Various characteristics of the transient response are shown in Table 7, Table 8, and Table 9. These values were calculated by passing the resistivity data into the built-in MATLAB®. function "stepinfo()" which calculates various characteristics of systems when a step input is applied.

Table 7. Max Resistivity

Max Resistivity [Ω·cm]		Applied Voltage [V]				
		5	7.5	10	15	20
Applied Stress [kPa]	1448	5019	2590	1456	1082	556
	926	14953	19259	3762	1157	852
	404	15524	20857	3238	2498	1696

Table 8. Percent Overshoot

Percent Overshoot		Applied Voltage [V]				
		5	7.5	10	15	20
Applied Stress [kPa]	1448	196	155	93.97	123	48
	926	121	620	301	110	129.6
	404	373	196.6	117	190	155

Table 9. Settling Time

95% Settling Time [hrs]		Applied Voltage [V]				
		5	7.5	10	15	20
Applied Stress [kPa]	1448	0.3	4.2	4.6	4.3	5.6
	926	4.7	1.5	0.8	5.0	3.6
	404	0.007	5.7	2.7	3.2	4.8

There are a few characteristics of the material that can be determined from Table 7, Table 8, and Table 9. First is that, in most instances, increasing the applied voltage decreases the percent overshoot of the resistivity. Again, this is likely attributed to the potential energy needed for an electron to tunnel. By exciting the system with higher voltage, the electrons in the system more quickly acquire enough energy to tunnel, which decreases the large initial resistance. Second is that, the settling times vary from 0.007 hours to as high as 5.7 hours. This is due to continuous creep of the material, which is a problem when working with any thermoplastic, as the MTS hydraulic press applies a constant load to the system. As the material continues to creep, the resistivity slightly decreases over long periods of time. However, in this carbon nanofiber composite, the virtual crosslinks of the polymer's hard domains, and pinning effect of the nanofibers help to limit creep of the composite.

4.1.2 Steady State Response

Perhaps the most important characteristic of the prototype pad is its steady state resistance. These values were determined by averaging the resistivity values of the material over the last four hours of testing. The results are shown in Table 10. These values reiterate the general trends seen throughout the experiments. That is, increasing the applied load, and

therefore stress on the material, as well as increasing the applied voltage decreases the resistivity of the material.

Table 10. Steady State Resistance

Steady State Resistivity [Ω cm]		Applied Voltage [V]				
		5	7.5	10	15	20
Applied Stress [kPa]	1448	1684	1039	763	500	390
	926	6774	2776	969	568.5	381
	404	14959	8034	1528	889	694

4.1.3 Transverse and Longitudinal Conductivity

For longitudinal and transverse testing, the interlock portion of an injection molded insert was removed. The sample was then loaded and tested along each axis in accordance with Section 2.1. The results of the conductivity tests are presented in Figure 31 and Figure 32.

Comparing the two figures, there is quite a significant difference in electrical resistivity of the material depending on the direction that is being tested. We can see that in the longitudinal direction, the resistance of the material is an entire order of magnitude less than in the transverse direction. From the mold flow simulation in Section 3.3, it is expected that the fibers in this location have a relatively strong alignment in the longitudinal direction. Studies have shown carbon nanofibers to be significantly more conductive along their axis, compared to the transverse direction. This alignment of nanofibers compounded with the fact that the fibers themselves are more conductive in that particular direction is what caused the significant decrease in resistivity. Furthermore, although the loading face and condition was slightly different, the resistivity for the transverse direction is near the conductivity of the prototype pad.

This is expected since in both scenarios the load and potential difference is being applied normal to the axis of the expected alignment of the CNFs.

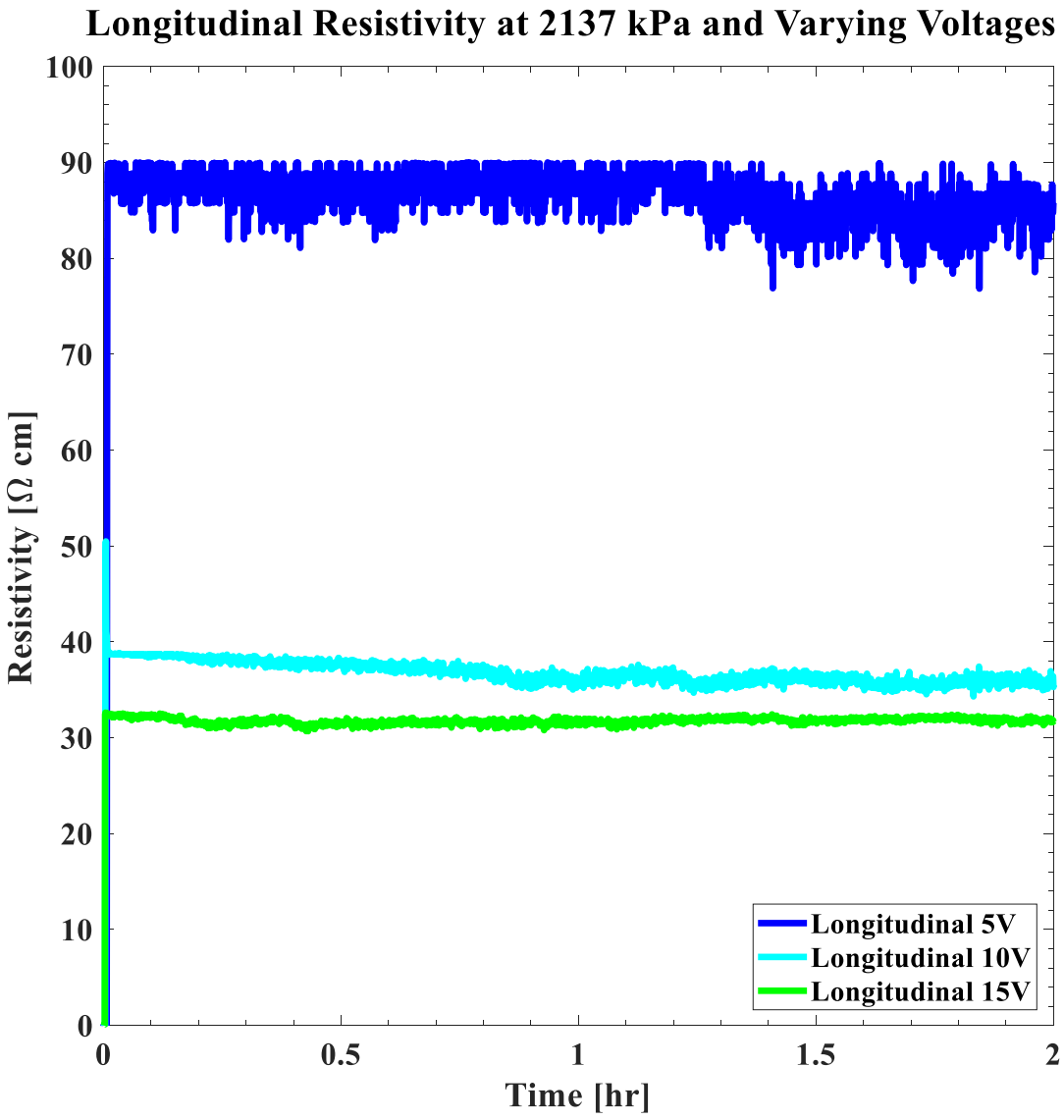

Figure 31. Longitudinal resistivity Testing

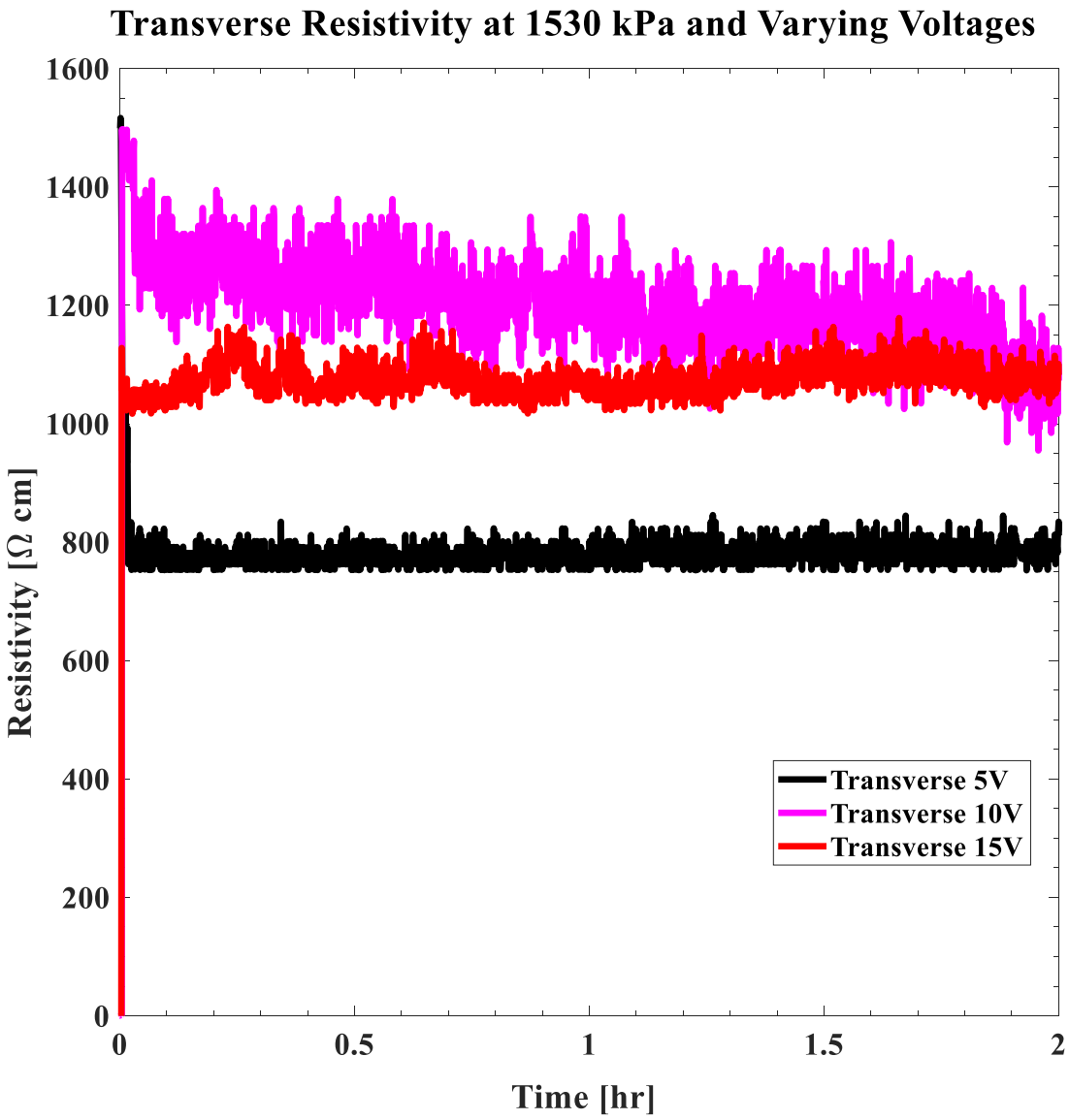

Figure 32. Transverse resistivity testing

4.2 X-Ray Diffraction

As previously mentioned, various samples were examined using X-ray diffraction spectroscopy in hopes of characterizing the hard domains, identifying differences in the material morphology, and estimating how these differences affect the composites resistivity as a whole. The results of the tests are shown in Figure 33.

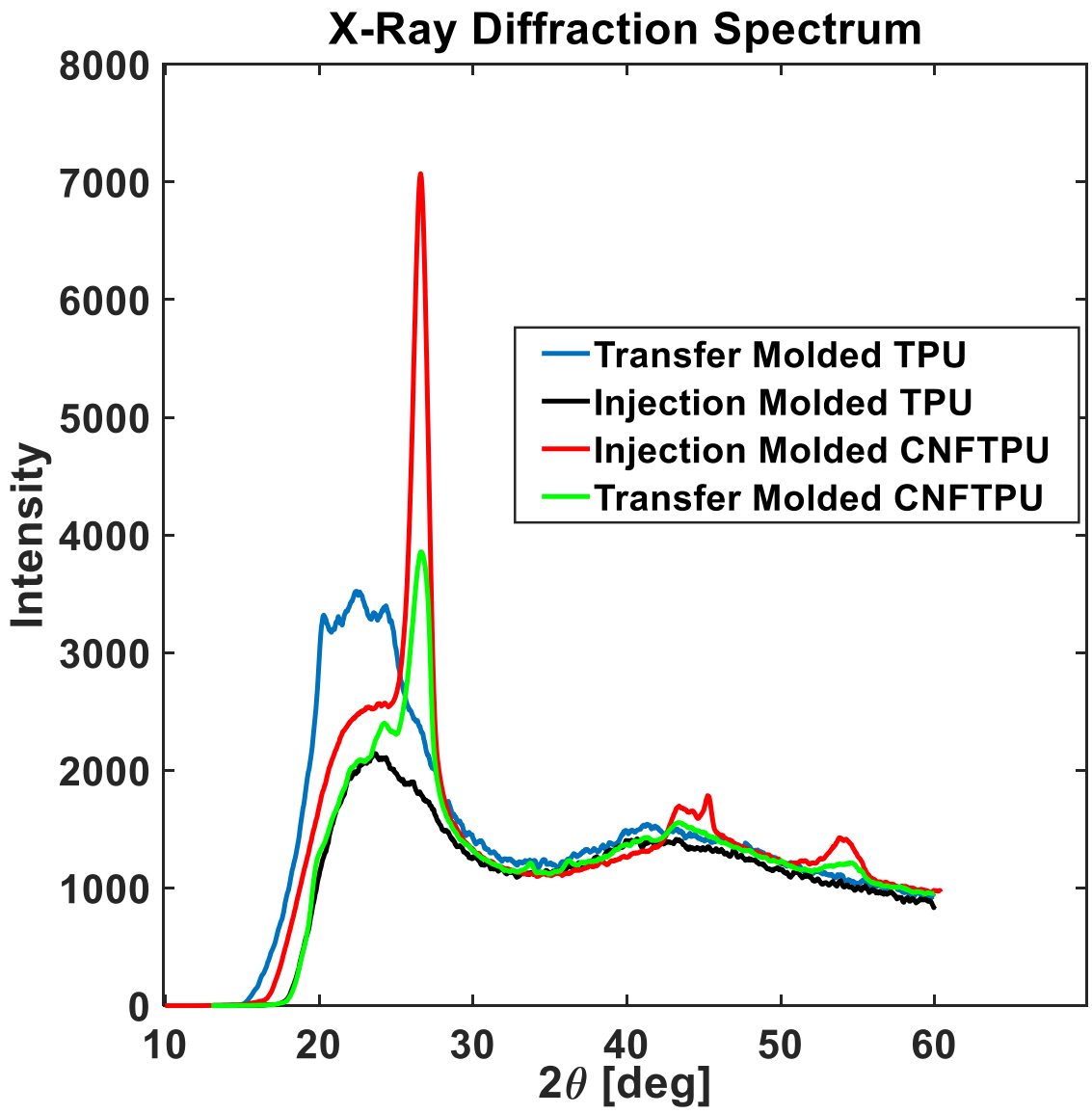

Figure 33. X-ray diffraction spectrum of TPU, and CNF/TPU composite manufactured via transfer-molding and injection-molding

From left to right, the first broad hump seen in all the samples is centered at approximately $2\theta = 22.5°$ and is characteristic of the BASF Elastollan TPU used in these experiments. This broad peak arises from the general association of hard segments within the TPU and is typical of most amorphous solids. There are however distinct differences in the

smoothness of each spectrum. That is, the samples that were created via transfer-molding are distinctly rougher than their injection-molded counterparts. In fact, the transfer-molded samples both have two additional small peaks at $2\theta = 20.3°$ and $2\theta = 24.3°$, respectively. These peaks are believed to be related to additional spherulites that are able to grow off the main hard segments as a result of the slow cooling rate seen by the transfer-molded samples. Specifically, the slow cooling rate allows the hard segments within the polymer the time and energy necessary to concentrate and form more distinct pseudo-crystals. Also, recall that the injection-molded CNF/TPU was mixed by Applied Sciences, Inc using a modified version of the Elastollan 1195a with slightly different hard domains, as well as their proprietary mixing procedure for conductive composites. The effect of the modified Elastollan can be seen by the larger magnitude of the broad peak when compared to both the transfer-molded composite, as well as the injection-molded neat Elastollan 1195a.

The peaks on both CNF/TPU curves are characteristic of the carbon nanofibers used as conductive fillers within the polymer. Both samples were compounded with Pyrograf® PR-19-XT-HHT carbon nanofibers and have a peak centered at $2\theta = 26.6°$. However, there is a significant difference in the magnitude of the peaks. One likely explanation for this, is that in the conductive transfer-molded parts, the pseudo-crystals associated with the 24.3° peak grew on and around the CNFs. This is seen in the figure as the slight overlap of the ends of the two distinct peaks. This interaction potentially weakened both the energy of the incoming X-rays, as well as the energy of the refracted X-rays.

As mentioned in section 1.3, the hard domains act as virtual crosslinks within the polymer. It is suspected, that when interlocked with the carbon nanofibers, they are able to limit movement not only of the soft segments, but also of the fibers as well. This makes it more likely

that fiber chains come into contact with each other under compressive loads rather than flow past each other with the polymer. This may be the reason that the transfer-molded composites tend to have enhanced electrical conductivity compared to the injection-molded samples.

4.3 Scanning Electron Microscope

Images from the scanning electron microscope are shown in Figure 34. The left image shows good dispersion of nanofibers throughout the sample with no visible agglomerations. Also, it can be observed that many of the fibers were able to maintain the relatively long lengths, on average between 5 μm and 7 μm, even through the shear intensive injection molding process. There is also a preferred orientation of the fibers. The first sample, being from the edge of a molded insert, has an orientation that is aligned with the plane of the mold as expected. However, the right image taken from the middle of the insert, also shows a tendency for the fibers to have a slightly preferred orientation. This subtle orientation is similar to what was expected in the center of the inserts as predicted by the mold flow analysis in Section 3.4. Also apparent from the right image is the good wetting of fiber by the polymer, as each fiber is completely embedded in polymer.

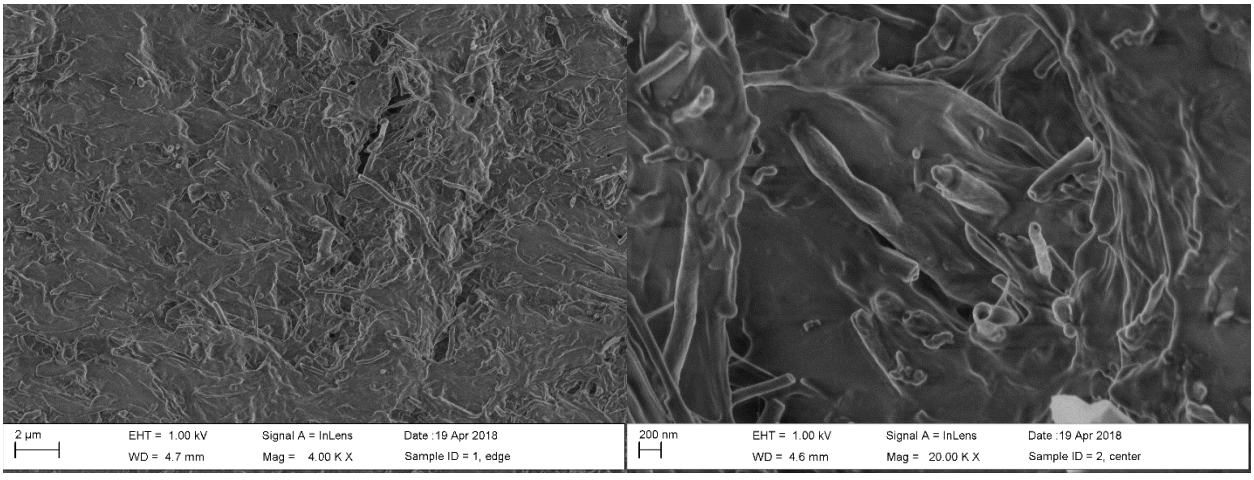

Figure 34. Scanning electron microscope images of TPU/CNF injection molded insert

4.4 Differential Scanning Calorimetry (DSC)

The test method for the DSC experiments performed was outlined in Section 2.4, but in short, a double run was utilized to determine the effects of processing conditions on the morphology of the samples. A DSC comparison of the injection-molded insert to the transfer-molded pucks is presented in Figure 35.

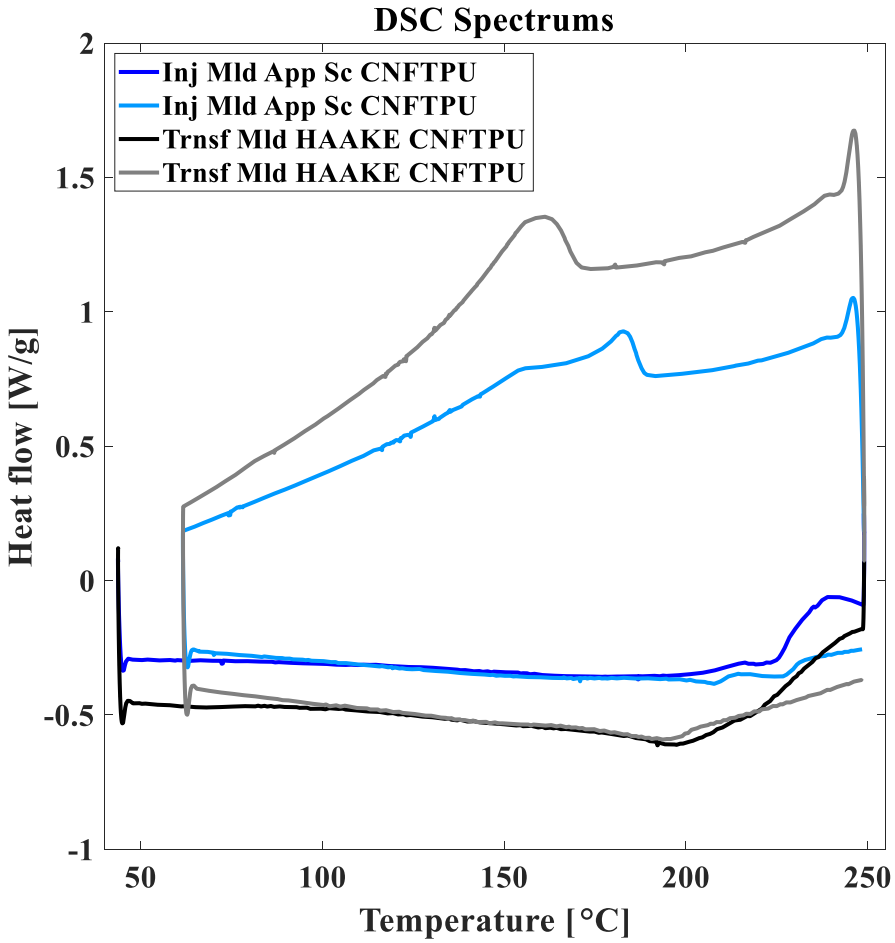

Figure 35. DSC comparison of injection-molded conductive insert to transfer-molded conductive puck

For the injection-molded sample, there does not appear to be any indications of a melt during the first run. The first significant change is a relatively large broad hump centered at

about 240°C. This hump is not repeated during the second run, so it is believed that this hump is caused by the composite material relaxation of molded-in strain relaxing when the temperature permits large scale molecular motions. As mentioned in Section 1.4, CNFs can act as pinning points within the polymer matrix. In this case, there is a small amount of residual stress that resulted from a combination of the pinning effects as well as the rapid cooling of the insert in the injection mold. For the transfer molded sample, there appears to be a small valley at 195°C that is associated with the melting point of the pseudo-crystals, as it is seen again on the second run. Again, there is an exotherm that is related to the stress relaxation, however, since the transfer-molded samples are already cooled at a relatively slow rate, this reaction has a lesser magnitude than for the injection molded sample. Following the first ramp up, the sample is cooled (upper portion of the curve). In both composites, there is a crystallization peak. For the injection-molded material this is near 180°C, and for the transfer-molded material there is a larger peak centered at 160°C. A higher crystallization temperature is typically desired for injection-molding processes so that material does not have to be held in the mold as long, reducing cycle times. In the second heating run, there is a small double melt for the injection-molded sample, and a very similar melt for the transfer molded sample. Lastly, both stress relaxation reactions shown in the first run are greatly reduced in both samples during the second run. This would be expected since the second run samples were cooled at extremely low rates, producing a near equilibrium molecular arrangement.

Figure 36 compares the morphology of the injection-molded conductive inserts against the injection-molded neat Elastollan 1195a. Interestingly, the neat Elastollan appears to have formed just slightly more pseudo-crystals in the molding process than the material with the CNFs as indicated by the two subtle dips near 200°C on the first run. This appears to be in contrast

with the results of the XRD testing. One possible explanation is that the modified Elastollan, used to make the conductive composites, had a larger association of hard segments, that is hard segments that are physically closer together indicated by the large hump in the XRD spectrum, but the standard Elastollan 1195a had more ordering of the hard segments, as indicated by the much rougher XRD scan. However, further information on the modified material is needed before a definitive answer can be offered.

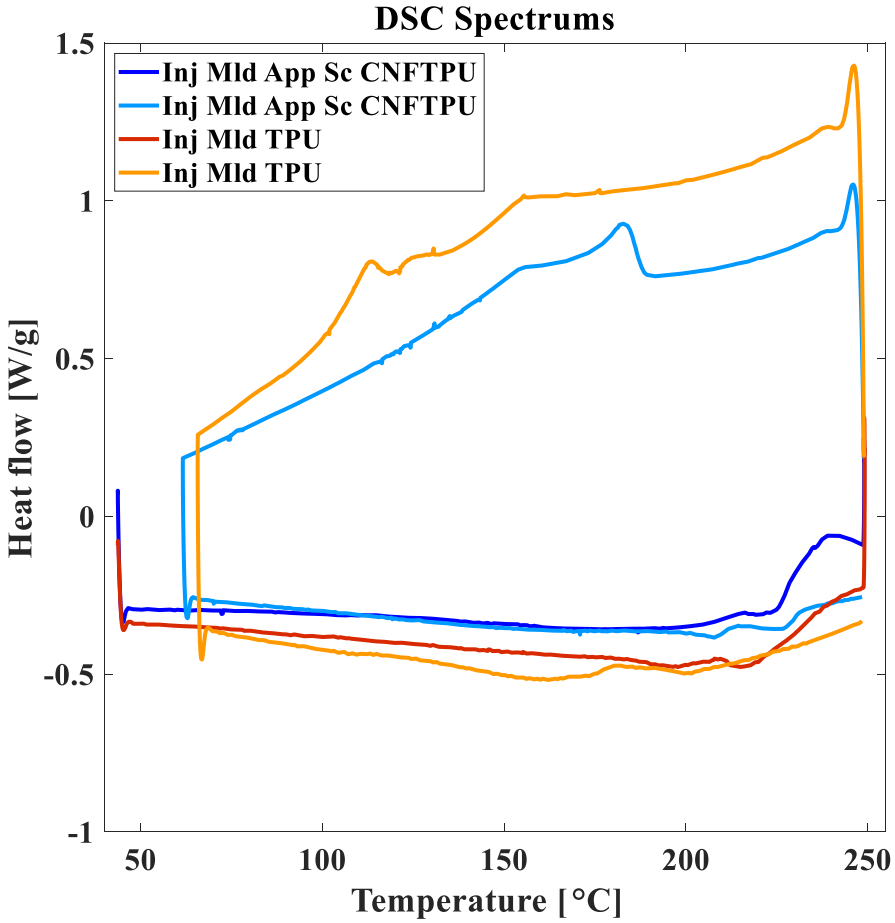

Figure 36. DSC comparison of injection-molded insert with and without CNFs

CHAPTER V

CONCLUSIONS AND RECOMMENDATIONS

This study successfully advanced previous work by creating a conductive polymer composite via injection-molding. This was accomplished by using a modified Elastollan 1195a TPU that had hard segments that would associate at lower temperatures, as well as minimizing the shear on the polymer and fibers when injection-molding. The effect of load and applied potential difference on the resistance of the material, as well as the difference in morphological structure between injection-molded and previously transfer-molded samples, was examined. A prototype steering pad was created by removing a section of the actual AdapterPlus™ steering pad and inserting an injection-molded part made of a blend of 15 weight percent carbon nanofibers and 85 weight percent modified Elastollan 1195a (TPU).

The electrical conductivity tests show that between 0 and 926 kPa of applied stress, the resistivity of the prototype pad decreases as the applied load on the pad increases. Above 926 kPa, increasing stress appears to have a diminishing effect on resistivity. Also analyzed in this study was the effect of voltage on the resistivity of the material. It was shown that the resistance has a non-linear dependence on the voltage, specifically, as the applied potential difference increases, the resistance of the material decreases. This is consistent with conductivity by percolation rather than direct contact and indicates that the fiber dispersion was very good.

The transient response is shown in these experiments mainly for academic purposes. It is interesting to note that the initial resistance of the pad when it is first loaded can be nearly twice

the steady-state value. Depending on the loading and voltage conditions, the settling time can vary from as little as 0.6 hours at high potential difference and high loads to nearly 1.5 hours at low potential differences and low loads. However, in practice, the pad will only see a zero load if the railcar itself momentarily loses contact with the wheel-axle assembly as a result of a significant bump in the rail tracks, so settling time will not be a major concern in actual service. Furthermore, the high initial resistance is likely due to surface resistance between the pad and metal fixtures.

Longitudinal and transverse conductivity tests demonstrated that there is an order of magnitude difference in conductivity depending on the preferred orientation of carbon nanofibers within the sample. This is a critical concept to keep in mind as the prototype pad continues to be optimized for service. One way to improve conductivity of the prototype pad is to optimize gate placement so that the fibers in the injection molded part are relatively aligned with the direction of the desired flow of electrical current.

From X-ray diffraction testing, it was seen that the injection-molded sample and the transfer-molded sample have similar overall morphological structure. However, the diffraction curve of the transfer-molded sample is slightly rougher, which suggests variations of hard segments within the polymer. Also, the nanofiber peak of the injection-molded sample is much larger than that of its transfer-molded counterpart. It is believed that this suggests slightly more alignment of nanofibers in the composite part, however, further testing is required to confirm this.

Future work planned for the pad includes testing the system under cyclic, or vibrating loads, as experienced in actual operation. Further work into the relationship between morphology and electrical conductivity is planned to better guide process optimization and future resin

development. Finally, resistance measurements will also be performed at a range of temperatures consistent with rail operations.

APPENDIX A

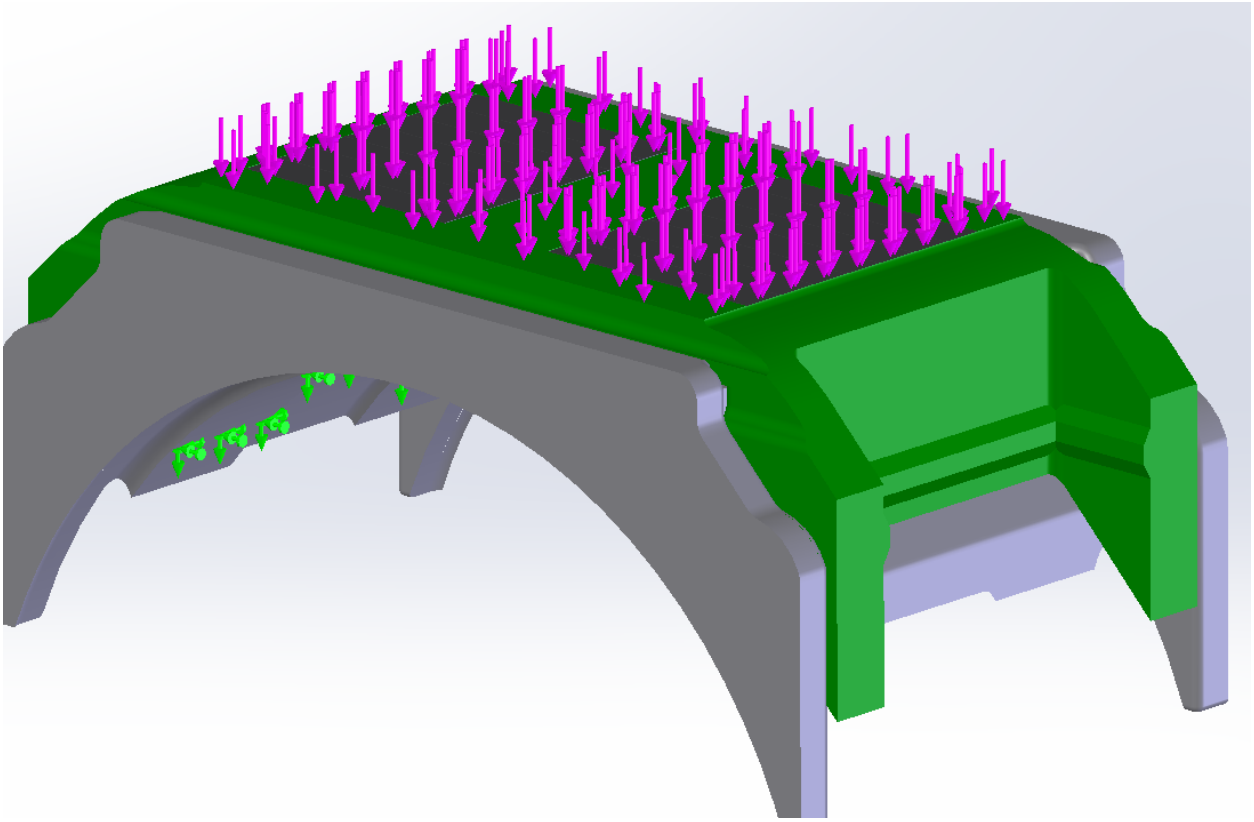

Figure 37. Finite element analysis of prototype pad

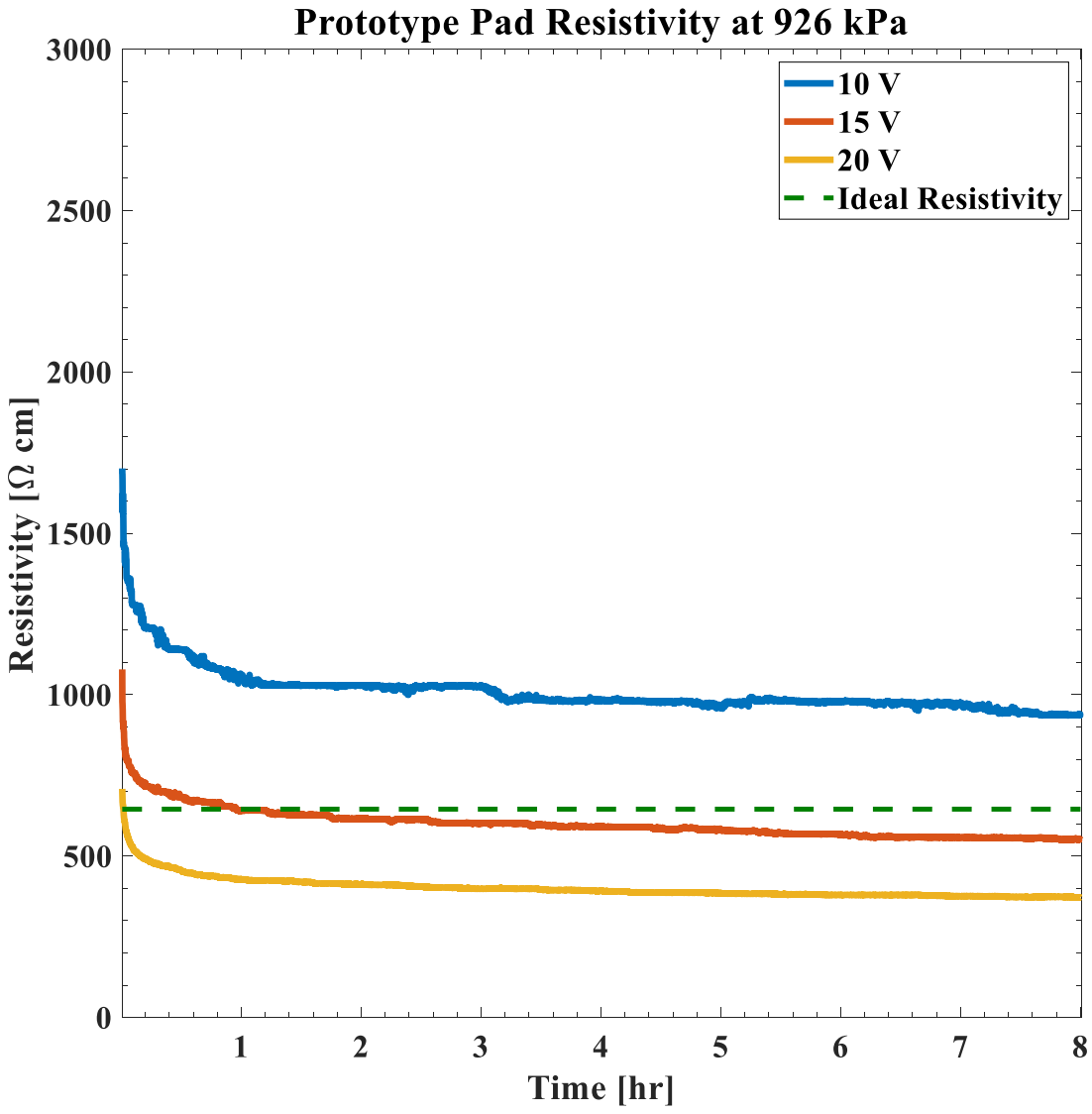

Figure 38. Prototype pad resistivity at 926 kPa and varying voltages

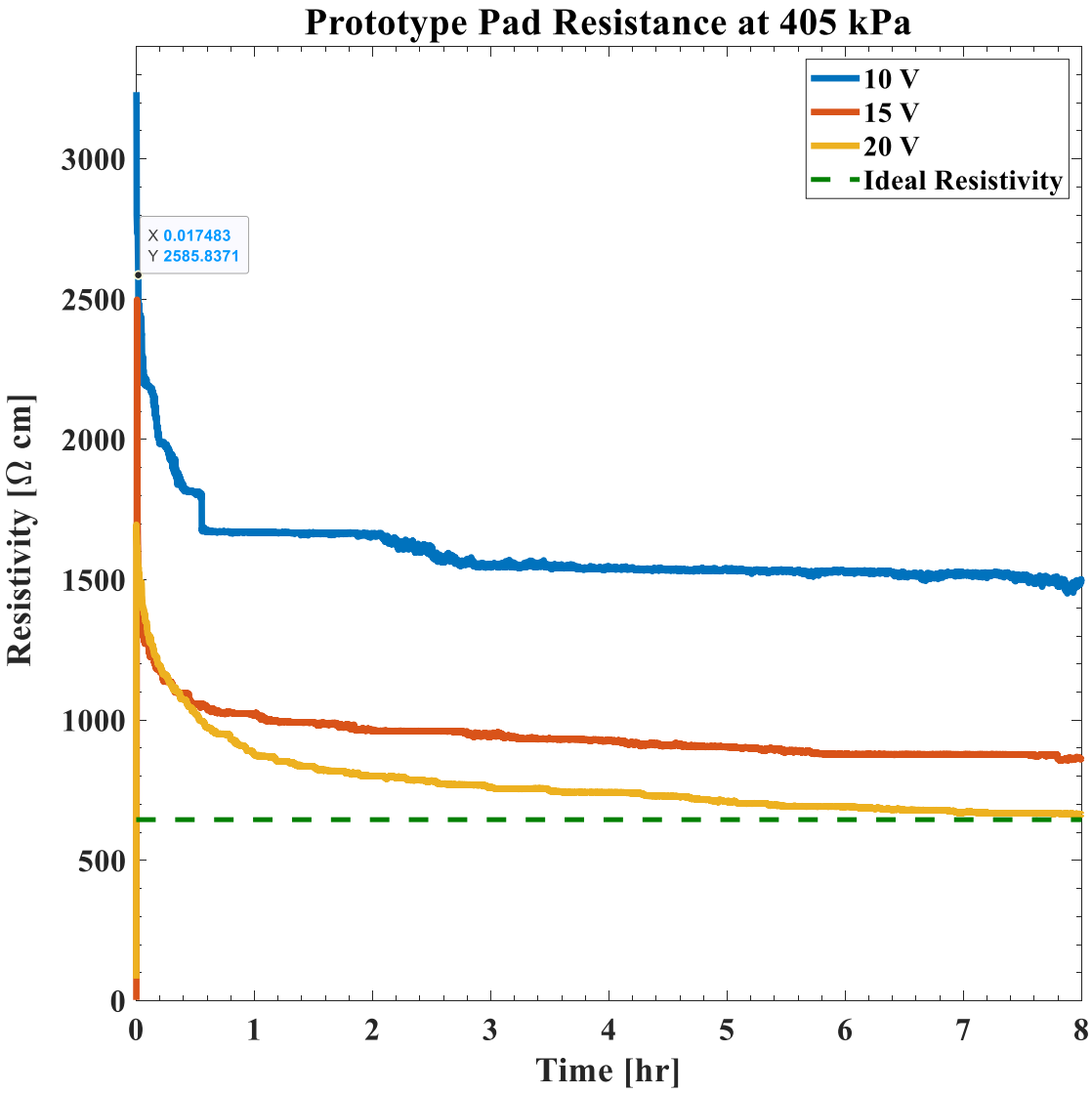

Figure 39. Prototype pad resistivity at 406 kPa and various applied voltages

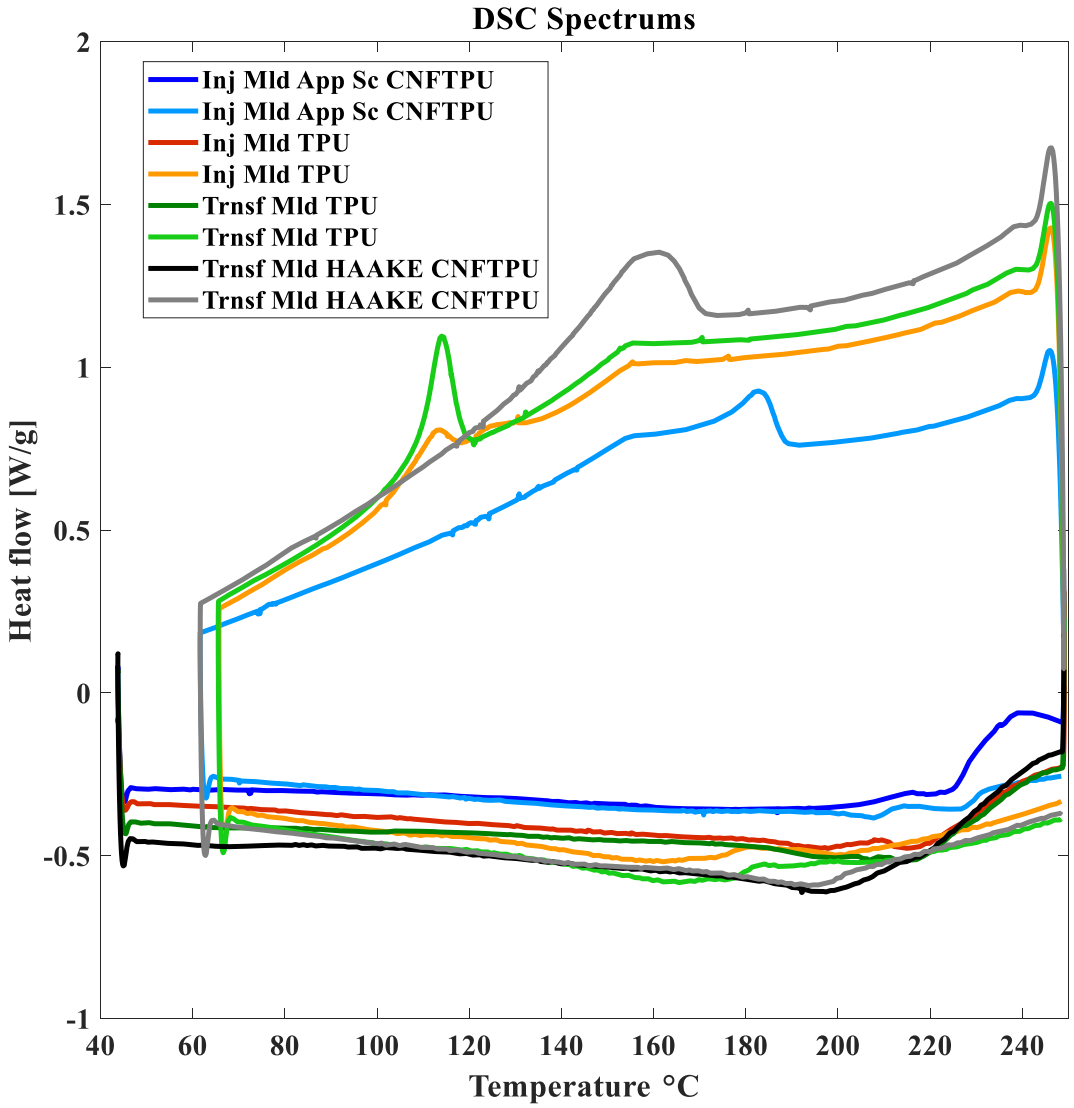

Figure 40. DSC plot for CNFTPU and neat TPU manufactured via injection-molding and transfer-molding

REFERENCES

[1] Amsted Rail, "AdapterPlus™Steering Pad System," 2012. [Online]. Available: http://www.amstedrail.com/. [Accessed 25 May 2015].

[2] Suarez, R., "Design and Optimization of a Railroad Conductive Suspension Element Pad Composed of Thermoplastic Polyurethane and Carbon Black," Master's Thesis, University of Texas Pan-American, August 2013.

[3] Basaldua, D. T., "Effects of Vapor Grown Carbon Nanofibers on Electrical and Mechanical Properties of a Thermoplastic Elastomer," Master's Thesis, University of Texas Pan-American, December 2014.

[4] BASF. Elastollan 1195A [Elastollan TPU Technical Data Sheet].

[5] Holden, G. Thermoplastic Elastomers. Third Edition. Munich: Hanser Publishers, 2004. Print.

[6] Drobny, J. G. Handbook of Thermoplastic Elastomers. Norwich, NY: PDLPlastics Design Library/William Andrew Pub., 2007. Print.

[7] "A Comparison of Carbon Nanotubes and Carbon Nanofibers." Pyrograf® ProductsInc. Applied Sciences, n.d. Web. 13 Nov. 2014.

[8] Al-Saleh, Mohammed H., and Sundararaj, Uttandaraman. "A Review of Vapor Grown Carbon Nanofiber/polymer Conductive Composites." Carbon 47.1 (2009): 2–22. Web.

[9] Deng, Hua, et al. "Progress on the Morphological Control of Conductive Network in Conductive Polymer Composites and the Use as Electroactive Multifunctional Materials." *Progress in Polymer Science*, vol. 39, no. 4, 2014, pp. 627–655., doi:10.1016/j.progpolymsci.2013.07.007.

[10] Ji, Mizhi, et al. "Selective Localization of Multi-Walled Carbon Nanotubes in Thermoplastic Elastomer Blends: An Effective Method for Tunable Resistivity–Strain Sensing Behavior." *Composites Science and Technology*, vol. 92, 2014, pp. 16–26., doi:10.1016/j.compscitech.2013.11.018.

[11] Barick, Aruna Kumar, and Deba Kumar Tripathy. “Effect of Nanofiber on Material Properties of Vapor-Grown Carbon Nanofiber Reinforced Thermoplastic Polyurethane (TPU/CNF) Nanocomposites Prepared by Melt Compounding.” *Composites Part A: Applied Science and Manufacturing*, vol. 41, no. 10, 2010, pp. 1471–1482., doi:10.1016/j.compositesa.2010.06.009.

[12] Cullity, B. D. *Elements of X-Ray Diffraction. 2.Ed*. Reading, Mass., Addison-Wesley, 1978, 1978.

[13] Britannica, The Editors of Encyclopaedia. “Bragg Law.” *Encyclopædia Britannica*, Encyclopædia Britannica, Inc., https://www.britannica.com/science/Bragg-law/media/1/76973/17859.

[14] Khursheed, A. (2011). Scanning electron microscope optics and spectrometers. Singapore ;: World Scientific Pub. Co.

[15] Choudhary O. Scanning Electron Microscope: Advantages and Disadvantages in Imaging Components. Int. J. Curr. Microbiol. App. Sci (2017) 6(5) 1877-82

[16] “Principle of Differential Scanning Calorimetry (DSC).” *Principle of Differential Scanning Calorimetry (DSC) : Hitachi High-Technologies GLOBAL*, www.hitachi-hightech.com/global/products/science/tech/ana/thermal/descriptions/dsc.html.

[17] Saenz, Lorenzo. Calibration and Optimization of a Load Sensor Embedded in a Railroad Bearing Adapter . 2013.

[18] “What Is Injection Moulding.” Aplusplastics, Aplusplastics, aplusplastics.com.au/about/what-is-injection-moulding/.

[19] Burton, D., Lake, P., and Palmer, A., “Carbon Nanofiber Applications and Properties,” Applied Sciences, Inc., n.d. Web. 13 Nov. 2014.

[20] Struempler, R., and Glatz-Reichenbach, J., “FEATURE ARTICLE Conducting Polymer Composites,” Journal of Electroceramics, 3 (4), 1999: pp. 329–346. DOI: https://doi.org/10.1023/A:1009909812823

[21] SEM and Imaging: The applications and practical uses of scanning electron microscopes. ATA scientific instruments . (2017). https://www.atascientific.com.au/sem-imaging-applications-practical-uses-scanning-electron-microscopes/

[22] Lou, Pengfei, et al. “Preparation and Structure of Rare Earth/Thermoplastic Polyurethane Fiber for X-Ray Shielding.” *Journal of Applied Polymer Science*, vol. 136, no. 17, 2018, p. 47435., doi:10.1002/app.47435.

BIOGRAPHICAL SKETCH

Anthony Alex Villarreal was born in Edinburg, Texas on March 30, 1994. He attended Edinburg North High school and graduated in the Spring of 2012. Afterwards, he attended the University of Texas Rio Grande Valley, where he graduated Magna Cum Lade with a bachelor's degree in Mechanical Engineering in the Spring of 2016. He was hired with Vaughn construction as a Quality Control Inspector, where he helped oversee construction of UTRGV's newest Science Building. In Spring 2018, he chose to continue his studies at the University of Texas Rio Grande Valley and obtained his Master of Science degree in Mechanical Engineering in August 2019. During this time, Anthony received an Award for Outstanding Graduate Student, co-authored a research paper and presented his findings at the 2019 Joint Rail Conference, and was named the 2019 Student of the Year for the University Transportation Center for Railway Safety. Anthony may be reached by email at anthony.a.villarreal@gmail.com.